J. Fluid Mech. (2026), *vol.* 1036, A30, doi:10.1017/jfm.2026.11604

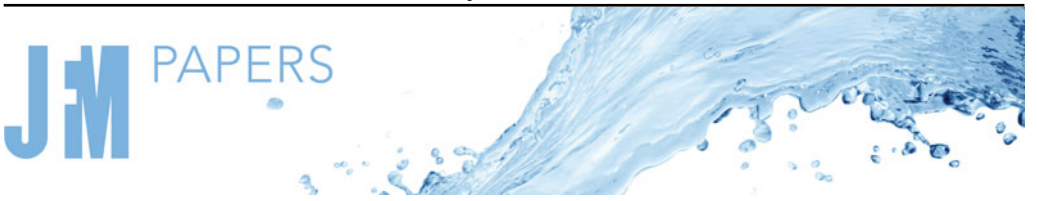

Mass transfer in drop-laden turbulent flow

Simone Di Giorgio[1,2], **Francesco Zonta**[3], **Sergio Pirozzoli**[4], **Alessandro Iafrati**[1] **and Alfredo Soldati**[2,5]

[1]Istituto di Ingegneria del Mare, Consiglio Nazionale delle Ricerche (INM-CNR), Via di Vallerano 139, Rome 00128, Italy

[2]Institute of Fluid Mechanics and Heat Transfer, TU-Wien, Geitreidmarkt 9, 1060 Vienna, Austria

[3]School of Engineering, Newcastle University, Newcastle upon Tyne NE1 7RU, UK

[4]Dipartimento di Ingegneria Meccanica e Aerospaziale, Sapienza Università di Roma, via Eudossiana 18, Rome 00184, Italy

[5]Department Politecnico di Ingegneria e Architettura, University of Udine, Udine 33100, Italy

Corresponding author: Simone Di Giorgio, simone.digiorgio@inm.cnr.it

(Received 15 October 2025; revised 24 March 2026; accepted 27 April 2026)

We employ direct numerical simulation coupled with a volume-of-fluid method to investigate mass transfer in drop-laden turbulent flows. In this set-up, drops initially saturated with a specific chemical species are injected into a turbulent channel flow where the species is initially absent. This configuration leads to mass transfer from the drops to the surrounding flow. Two distinct sets of numerical simulations are conducted. In the first set, we vary the Schmidt number (Sc) of the carrier fluid while maintaining a unity diffusivity ratio between the carrier fluid and the drops. In the second set, we keep the Schmidt number inside the drops constant and systematically vary the diffusivity ratio, D_r. Our results show that, regardless of the value of the diffusivity ratio D_r, the mass-transfer velocity $\mathcal{K}$ (or equivalently, the Sherwood number Sh, which represents the ratio of convective to diffusive mass-transfer rates), with $\mathcal{K} \propto Sh/Sc$, scales as $\mathcal{K} \sim Sc^{-1/2}$. This result, which is consistent with many theoretical, experimental and numerical predictions found in the literature and covering a broad spectrum of instances (i.e. gas–liquid and liquid–liquid flows), seems to highlight a universal nature of the mass-transfer process across fluid interfaces. Interestingly, while the diffusivity ratio D_r does not influence the scaling $\mathcal{K} \sim Sc^{-1/2}$, it does influence the magnitude of the mass-transfer velocity. In particular, and for the range of D_r considered here ($1 < D_r < 400$), we show that $\mathcal{K}_{D_r>1}/\mathcal{K}_{D_r=1} \simeq 1.75$. These findings are further explained using a simple lumped-parameter model of the process. We anticipate that these insights

will contribute to the development of more accurate models and parametrisations in the field of mass transfer in turbulent dispersed flows.

Key words: breakup/coalescence, mass transport, turbulent flows

1. Introduction

Mass transfer in drop-/bubble-laden turbulent flows is a key process in a wide range of fields, from environmental and atmospheric sciences (Emerson & Bushinsky 2016; Deike 2022) to process engineering (Kokal 2005; Risso 2018). Examples include oxygenation in water bodies, carbon dioxide (CO_2) absorption and pollutant removal – influencing aquatic ecosystems and climate regulation – but also mixing in chemical reactors, two-phase heat exchangers and emulsions (Pelusi *et al.* 2023). Whether in the upper layers of the ocean, or in a chemical reactor, the presence of drops/bubbles in a turbulent flow significantly influences the efficiency of mass transfer between phases (Xu *et al.* 2008). The problem of mass transfer in drop-/bubble-laden turbulence is, however, extremely complicated to study. Beyond the complexity of capturing the dynamics of the turbulent carrier phase in large-scale inherently inhomogeneous flows (which is itself rather challenging) we have to consider the presence of a second dispersed phase – i.e. a drop – with its own thermophysical/physicochemical properties, which can indeed be very different compared with those of the carrier phase. In addition, the two phases are separated by an interface that can deform according to the behaviour of the surrounding turbulent flow, and that can change topology (i.e. coalescence and breakage events). It is therefore not surprising that the characterisation of the mass transfer at a fluid interface requires the evaluation of many parameters, the most important of which are the Reynolds number Re, a measure of the inertia to viscous forces ratio, the Weber number We, a measure of the inertia to surface tension forces ratio, the Schmidt number Sc, a measure of the momentum to mass diffusivity ratio, and the Sherwood number Sh, a measure of the mass-transfer rate. Note that, in particular in the context of geophysical/environmental applications, Sh is often replaced by the gas transfer velocity, $\mathcal{K} \sim Sh/Sc$. Because of the many practical applications, the literature in the field of mass transfer through interfaces is vast, and can be dated back to the seminal work of Boussinesq (1905) and Levich (1962) on theoretical/analytical prediction of the mass transfer at the interface of an isolated bubble rising in a quiescent liquid. Many other semi-empirical/analytical studies have followed (see Kumar & Hartland (1999) for a comprehensive review), which typically apply to simplified cases of isolated/undeformable drops/bubbles immersed in quiescent or steady flows, and usually provide the value of Sh based on the specific flow configuration and on the value of Re and Sc. Semi-empirical/analytical approaches are naturally not possible for large numbers of drops/bubbles. In such cases, the most common approach is to consider many small undeformable drops/bubbles of sub-Kolmogorov size, which are dispersed into the flow and are tracked as material points via a Lagrangian approach (Kuerten 2016). When the drops/bubbles are large and are immersed in a turbulent flow, the problem becomes much more complicated, since the drops/bubbles can change shape and topology according to the external turbulent flow field. Even in this case, semi-analytical and theoretical predictions are not very reliable, and accurate experiments are particularly challenging to perform. Only recently, and because of the development of laser-induced fluorescence methods and similar optical techniques, experimental measurements of mass-transfer processes in bubble-laden turbulence have become available (Dani, Guiraud & Cockx 2007; Francois *et al.* 2011; Colombet *et al.* 2011, 2015). These techniques are, however, generally suitable for providing insightful information on integral/global quantities only, given the intrinsic difficulty in capturing the distribution of

scalar concentration and gradients at fluid interfaces that can deform, break and coalesce. For this reason, high-fidelity numerical simulations remain particularly attractive (see e.g. Méès *et al.* 2020; Dodd *et al.* 2021; Scapin *et al.* 2022; Hidman *et al.* 2023). Nevertheless, most of these simulations focus on a single drop/bubble immersed in a turbulent flow, with the remarkable exception of the work by Hidman *et al.* (2023), which focused on the transport of a passive scalar, subject to an externally imposed mean scalar gradient, in an unbounded, bubble-induced turbulent flow, in which bubble coalescence/interaction is prevented. To the best of our knowledge, there is no systematic study on the problem of mass transport in drop-laden wall-bounded turbulence, and focusing in particular on the influence of the diffusivity ratio between drops/bubbles and carrier flow. With the present study, we start bridging this gap. Specifically, we consider a drop-laden turbulent channel flow, and we perform a series of direct numerical simulations (DNS) of the mass-transfer process occurring between the drops and the turbulent carrier flow. Simulations are run using an incompressible Navier–Stokes solver coupled with a volume-of-fluid (VOF) method tailored for tracking the dynamics of the drop interface. Central in our study is the modelling of the species transport within the flow, which we have accomplished via the definition of an *ad hoc* advection–diffusion equation. This equation is suitable to account for different diffusivity and solubility between the two phases (drops and carrier flow) and to incorporate the solubility of the solute within the carrier phase. Overall, the employed methodology allows for a detailed evaluation of the interfacial mass transfer and a detailed analysis of the underlying physical processes influencing it, providing new insights into the mass-transfer process in turbulent multiphase flows.

In agreement with previous theoretical predictions (Bird 2002; Wylock, Colinet & Haut 2012), we show that different regimes for mass transport at a deformable interface are possible, which depend on the dispersed phase (subscript 'd') to carrier fluid (subscript 'c') diffusivity ratio $D_r = D_d/D_c$ (assuming a unitary equilibrium concentration ratio across the interface, $\alpha = C_b^{eq}/C_c^{eq} = 1$). Attention is here focused at the regime in which the mass-transport resistance inside the drop has little influence, $\sqrt{D_r} \gg 1$, and at the coupled regime, $\sqrt{D_r} \simeq 1$, in which the mass-transport resistance in both phases is important. A third regime, $\sqrt{D_r} \ll 1$, in which the mass-transport resistance outside of the drop has little influence, would be possible, though not of interest in the context of the present work.

2. Methodology

The DNS of turbulence is coupled with the VOF method to study the mass-transfer process in a drop-laden turbulent Poiseuille channel flow. In dimensionless form, the governing equations are

$$\frac{\partial \chi}{\partial t} + \boldsymbol{u} \cdot \boldsymbol{\nabla} \chi = 0, \tag{2.1}$$

$$\boldsymbol{\nabla} \cdot \boldsymbol{u} = 0, \tag{2.2}$$

$$\frac{\partial \boldsymbol{u}}{\partial t} + \boldsymbol{\nabla} \cdot (\boldsymbol{u}\boldsymbol{u}) = \frac{1}{\rho}\left[-\boldsymbol{\nabla} p + \frac{1}{Re}\boldsymbol{\nabla} \cdot \left(\mu\left(\boldsymbol{\nabla}\boldsymbol{u} + \boldsymbol{\nabla}\boldsymbol{u}^T\right)\right) + \frac{1}{We}\boldsymbol{f}_\sigma\right] + \Pi \boldsymbol{i}, \tag{2.3}$$

where χ is the phase indicator, $\boldsymbol{u} = \boldsymbol{u}(\boldsymbol{x}, t)$ is the fluid velocity, $p = p(\boldsymbol{x}, t)$ is the pressure, $\rho = \rho(\boldsymbol{x}, t)$ is the density, $\mu = \mu(\boldsymbol{x}, t)$ is the dynamic viscosity, $\boldsymbol{f}_\sigma$ is the surface tension force and Π is the pressure gradient applied to keep constant the mass flow rate along the streamwise direction (versor $\boldsymbol{i}$). The surface tension force is modelled as a volumetric force (continuum surface force model) concentrated at the interface:

$$\boldsymbol{f}_\sigma = k\delta_D\left(\boldsymbol{x} - \boldsymbol{x}_s\right)\boldsymbol{n}, \tag{2.4}$$

where $\boldsymbol{n}$ is the unit normal of the interface, k is the local curvature of the interface between the two fluids, while δ_D is the Dirac function that identifies the interface location and that is used to localise the force at the interface only, $\boldsymbol{x}_s$ (Tryggvason, Scardovelli & Zaleski 2011). The local curvature k is evaluated through the height function method, which mitigates spurious currents. Further details of the implementation and validation of this method are reported in Di Giorgio *et al.* (2024) and Rossi *et al.* (2025).

Flow parameters that appear in (2.3), *Re*, *We* and *Sc*, are the Reynolds, Weber and Schmidt numbers, which are defined as

$$Re = \frac{\tilde{U}\tilde{L}\tilde{\rho}}{\tilde{\mu}}, \quad We = \frac{\tilde{\rho}\tilde{U}^2\tilde{L}}{\sigma}, \quad Sc = \frac{\tilde{\mu}}{\tilde{\rho}\tilde{D}}, \tag{2.5}$$

with σ the surface tension coefficient and $\tilde{\rho}$, $\tilde{\mu}$, $\tilde{D}$, $\tilde{L}$ and $\tilde{U}$ the reference values for density, dynamic viscosity, mass diffusivity, length and velocity, respectively.

In the VOF method, the phase indicator χ accounts for the volume fraction of one of the two phases (e.g. phase 1), and the local density and viscosity are then defined as

$$\rho = \rho_1\chi + (1-\chi)\,\rho_2, \quad \mu = \mu_1\chi + (1-\chi)\,\mu_2. \tag{2.6}$$

In the present work, (2.1), describing the transport of the phase indicator, is discretised with the geometric VOF method proposed by Weymouth & Yue (2010). The Navier–Stokes equations, (2.2)–(2.3), are solved with a projection method, in which the momentum equation is first advanced in time ignoring the pressure gradient; an intermediate velocity field, not satisfying the continuity equation, is then obtained; and a correction step is finally implemented, during which the pressure gradient is determined by enforcing the continuity equation, and then added to the intermediate velocity field to find the correct velocity field (Chorin 1968; Orlandi 2012). Time integration is carried out by means of the Adams–Bashforth explicit scheme for the convective terms and for the off-diagonal part of the viscous terms, while a Crank–Nicolson scheme is used for the diagonal diffusion terms.

2.1. *Advection–diffusion equation for species concentration*

The time evolution of the jth species concentration for phase 1 or phase 2, $c_{1/2,j}$, is given by (Standart 1964; Haroun, Legendre & Raynal 2010)

$$\frac{\partial c_{1/2,j}}{\partial t} + \boldsymbol{\nabla}\cdot\left(\boldsymbol{u}c_{1/2,j}\right) = -\boldsymbol{\nabla}\cdot\left(\boldsymbol{J}_{1/2,j}\right), \tag{2.7}$$

where $\boldsymbol{J}_{1/2,j}$ is the flux of species. The continuity of $\boldsymbol{J}_{1/2,j}$, across the interface Σ (Standart 1964; Bothe & Fleckenstein 2013), with the additional constraint that the transported species is dilute and does not induce volume change, reduces to

$$\boldsymbol{J}_{1,j}\cdot\boldsymbol{n}_\Sigma = \boldsymbol{J}_{2,j}\cdot\boldsymbol{n}_\Sigma. \tag{2.8}$$

Assuming continuity of chemical potentials at the interface Σ, which is a suitable choice in most applications, Henry's law is recovered:

$$c_{1,j} = c_{2,j}\alpha_j, \tag{2.9}$$

where the dimensionless ratio of the concentration of the transported species in phase 1 (e.g. the liquid phase) and in phase 2 (e.g. the gas/liquid phase), α_j, is called the Henry's law solubility constant (Sander 2023), and is simply referred to as solubility hereinafter (we refer the reader to Bothe & Fleckenstein (2013) for a deeper discussion about local chemical equilibrium and the generalised Henry's law). To avoid the introduction of further complexity in the system, the solubility α_j, which is in general a function of

temperature and pressure, is assumed to be constant in this study. In the context of the one-fluid formulation (Tryggvason *et al.* 2011; Roccon, Zonta & Soldati 2023), the species concentration and flux, which are valid for both phases 1 and 2 and for the chemical species j, can be written as

$$c_j = \chi c_1 + (1-\chi)c_2, \quad \boldsymbol{J}_j = -\left(\chi D_{j,1}\nabla c_1 + (1-\chi)\, D_{j,2}\nabla c_2\right). \tag{2.10}$$

The diffusivity at the interface is calculated using the harmonic mean of the two diffusivities of the species inside and outside of the drop, $D_{j,1}$ and $D_{j,2}$, respectively, to give (Haroun *et al.* 2010)

$$D_j = \frac{D_{j,1} D_{j,2}}{D_{j,1}\,(1-\chi) + D_{j,2}\chi}. \tag{2.11}$$

This finally leads to a single equation for species transport in both phases, which in dimensionless form reads as

$$\frac{\partial c_j}{\partial t} + \boldsymbol{\nabla}\cdot\left(\boldsymbol{u} c_j\right) = \frac{1}{ReSc}\boldsymbol{\nabla}\cdot\left(D_j\nabla c_j - D_j\left(\frac{c_j\left(\alpha_j-1\right)}{\alpha_j\chi + (1-\chi)}\right)\nabla\chi\right). \tag{2.12}$$

The convective term of (2.12) is discretised with an upwind-biased total variation diminishing scheme (see Pirozzoli *et al.* 2019) with the Arora and Roe limiter (Arora & Roe 1997), designed in such a way as to recover third-order accuracy in smooth regions. The term on the right-hand side of (2.12) is discretised with a backward Euler scheme, and the resulting linear system is solved with a multigrid method (Farsoiya, Popinet & Deike 2021). Validation tests of the numerical model adopted for the mass transfer are reported in Appendix A for the diffusion process from static and rising bubbles, while a further application of this implementation is given in Di Giorgio, Pirozzoli & Iafrati (2025).

3. Numerical simulations

The turbulent channel flow simulations are run imposing a constant mass flow rate. The size of the computational domain is $L_x \times L_y \times L_z = 4\pi h \times 2h \times 2\pi h$ in the streamwise, wall-normal and spanwise directions, respectively, with h the half-channel height. Hereinafter, and for ease of notation, we use the subscript 'd' to refer to the dispersed phase and the subscript 'c' to refer to the carrier flow. All simulations are initialised by injecting two regular, planar distributions of spherical drops into a fully developed turbulent flow. The drops have a diameter of $d = 0.4h$ with their centres located at a distance of $y_{b,0} = 0.5h$ from the top and bottom walls, respectively (128 drops in each planar distribution). The volume fraction of the drops is $V_d/(V_d + V_c) = 5.4\,\%$, with V_d and V_c the total volume of the drops and of the carrier phase, respectively. The initial condition of the species concentration field is such that all drops are initially saturated with an initial concentration $c_d = 1$, while the carrier phase is initially empty with an initial concentration $c_c = 0$.

We recall that the problem of mass transfer in a two-phase turbulent flow is governed by a number of physical parameters: the Reynolds number Re, the Weber number We, the viscosity ratio ($\mu_r = \mu_d/\mu_c$), the density ratio ($\rho_r = \rho_d/\rho_c$), the Schmidt number Sc, the diffusivity ratio $D_r = D_d/D_c$ and the solubility ratio $\alpha_j = C_d^{eq}/C_c^{eq}$, i.e. the ratio between the chemical species equilibrium concentration in the dispersed phase and in the carrier flow. Since our objective is to understand how the diffusivity of species influences the overall mass transfer, we keep all the parameters constant, but Sc and D_r. In particular, we assume $\mu_r = 1$, $\rho_r = 1$ and $\alpha_j = 1$. In addition, indicating with u_b the bulk velocity, and with the reference velocity and length scales given by $\tilde{U} = 2u_b$ and

Case	Sc_c	D_r	α_j	Re_b	We	$N_x \times N_y \times N_z$	Δx^+	$\Delta y^+_{min,max}$	Δz^+
A1	0.5	1	1	10 000	3100	$1152 \times 289 \times 576$	3.27	0.046–3.06	3.27
A2	1.0	1	1	10 000	3100	$1152 \times 289 \times 576$	3.27	0.046–3.06	3.27
A3	2.0	1	1	10 000	3100	$1152 \times 289 \times 576$	3.27	0.046–3.06	3.27
A4	4.0	1	1	10 000	3100	$1152 \times 289 \times 576$	3.27	0.046–3.06	3.27
B1	0.5	50	1	10 000	3100	$1152 \times 289 \times 576$	3.27	0.046–3.06	3.27
B2	1.0	100	1	10 000	3100	$1152 \times 289 \times 576$	3.27	0.046–3.06	3.27
B3	2.0	200	1	10 000	3100	$1152 \times 289 \times 576$	3.27	0.046–3.06	3.27
B4	4.0	400	1	10 000	3100	$1152 \times 289 \times 576$	3.27	0.046–3.06	3.27

Table 1. Overview of the main simulation parameters. We run two series of simulations: case A simulations, where the Schmidt number of the carrier phase is varied from $Sc_c = 0.5$ to $Sc_c = 4$, and is equal to the Schmidt number inside the drops, so that the diffusivity ratio is $D_r = 1$; and case B simulations, where the Schmidt number of the carrier phase is varied from $Sc_c = 0.5$ to $Sc_c = 4$, while the Schmidt number inside the dispersed phase is kept constant, $Sc_d = 0.01$ (i.e. D_r is increased from 50 to 400). The values of Sc, D_r and α_j are explicitly given. For all simulations, $\mu_r = 1$, $\rho_r = 1$.

$\tilde{L} = h$, we obtain $Re = 10\,000$ and $We = 3100$. The corresponding values of the shear Reynolds and Weber numbers are $Re_\tau = u_\tau h/\nu \approx 300$ and $We_\tau = \rho u_\tau^2 h/\sigma \approx 2.79$, since $Re_\tau \approx 0.09 Re^{0.88}$ (Pope 2001).

These values are representative of a physical situation characterised by a water and oil liquid–liquid mixture, with $\sigma \simeq 3 \times 10^{-3}$ N m^{-1}, in a channel with characteristic velocity $\tilde{U} \simeq 1$ m s^{-1} and characteristic length $h \simeq \mathcal{O}(10^{-2})$ m (see Than *et al.* 1988). Regarding the choice of Sc and D_r, we analyse two different situations: (i) the Schmidt number of the carrier phase is varied from $Sc_c = 0.5$ to $Sc_c = 4$, and is equal to the Schmidt number inside the dispersed phase, so that the diffusivity ratio is $D_r = 1$ (case A); (ii) the Schmidt number of the carrier phase is varied from $Sc_c = 0.5$ to $Sc_c = 4$, while the Schmidt number inside the dispersed phase is kept constant, $Sc_d = 0.01$, so that the diffusivity ratio is systematically increased from 50 to 400 (case B). The complete list of simulations performed in the present study is given in table 1. The computational grid is uniform in the streamwise and spanwise directions, where the flow is periodic, while it is non-uniform in the wall-normal direction (no-slip condition), along which the natural grid stretching proposed by Pirozzoli & Orlandi (2021) is used to cluster computational points near the walls. In wall units (obtained using ν/u_τ as reference length), the grid resolution for each case is $\Delta x^+ = \Delta z^+ \approx 3.27$, while Δy^+ ranges between 0.046 and 3.06, enough to solve the characteristic length scale of turbulence (the Kolmogorov scale, η_k) (Bernardini, Pirozzoli & Orlandi 2014). When a scalar is transported in a turbulent flow, a second characteristic length scale is present, the Batchelor scale, $\eta_B^+ = \eta_k^+/\sqrt{Sc}$, with Sc the Schmidt number (Batchelor 1959). Naturally, when $Sc = 4$, $\eta_B^+ = (1/2)\eta_k^+$. In the context of our simulations, and specifically to tackle this aspect, the employed computational grid (with $\Delta x^+ = \Delta z^+ = 3.27$ and $\Delta y^+ < 3.06$), which is over-refined for the flow field (i.e. to capture η_k^+), is perfectly suitable also for the scalar. Further details of the grid sensitivity analysis are given in Appendix A.3.

4. Results

Mass transfer in a drop-laden turbulent flow is a complex, hierarchical process. The building block of this process is represented by the dynamics of each drop: each drop interacts with local turbulence, which induces drop deformation and internal circulation; but at the same time each drop interacts with the other drops in a collective, large-scale,

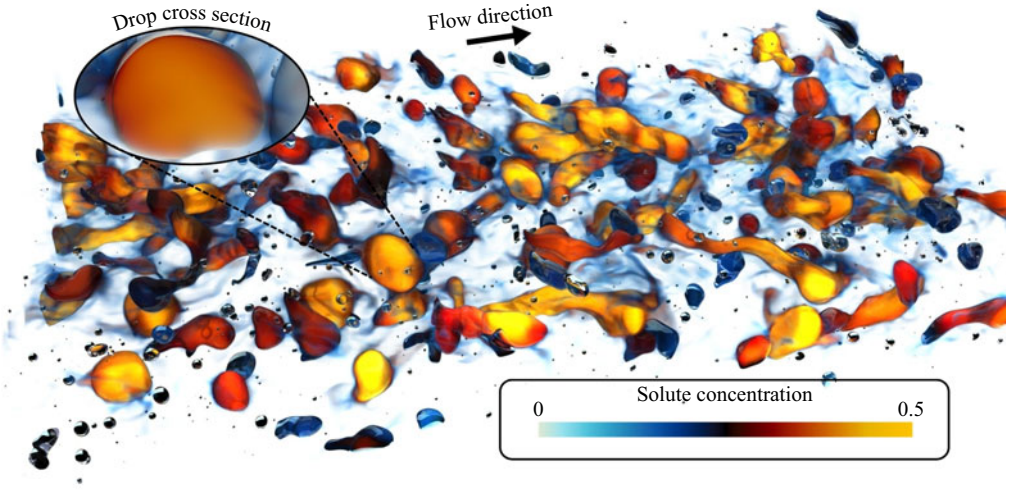

Figure 1. Three-dimensional rendering of mass transport in a drop-laden turbulent channel flow. The colour scale represents species concentration: yellow indicates high concentration, while blue indicates low concentration. The flow, driven by a pressure gradient, moves from left to right. The inset shows a cross-section of a drop, illustrating the internal distribution of species concentration. Results correspond to case B2, with $Sc = 1$, $D_r = 100$.

dynamics. This is visualised in figure 1, where a snapshot of the drop shape and location is given, together with a volume-rendering representation of the solute concentration (from yellow – high – to cyan – low – solute concentration). In an effort to clarify further the main ingredients of this dynamics, we focus on a single drop, immersed in turbulence, which comes closer to another drop. The situation is sketched in figure 2, via a sequence of snapshots representing two individual drops in the process of merging, for two different values of the molecular diffusivity inside the dispersed phase (case A2 and case B2 in table 1). We recall that the efficiency of the mass-transfer process crucially depends on the value of the molecular diffusivity of either fluid (here represented by its dimensionless counterpart, the Schmidt number, Sc). For case A2, shown in the top two rows of figure 2, the value of the Schmidt number outside and inside of the dispersed phase is the same and it is equal to $Sc_c = Sc_d = 1.0$. For case B2, shown in the bottom two rows of figure 2, the value of the Schmidt number outside of the drop is $Sc_c = 1.0$ while the value inside the drops is $Sc_b = 0.01$ (i.e. much larger diffusivity, typical of gases). We start by considering case A2. Two drops, one characterised by a higher species concentration (orange-to-yellow inner colour) and one by lower concentration (blue inner colour), merge. Because of the relatively low species diffusivity inside the drop ($Sc_d = 1.0$), species transport from the very beginning ($t^+ = 295$) is mainly due to advection. When the two drops merge, the species transport is still dominated by advection, and the mixing inside the newly formed drop is not very efficient (due to the relatively small characteristic size of the drop), and the resulting species concentration is inhomogeneous and characterised by larger gradients and fluctuations (see snapshots between $t^+ = 310$ and $t^+ = 375$). We now move to case B2, in which the species diffusivity inside the drop is much larger than outside the drop ($Sc_d = 0.01$, $Sc_c = 1.0$). At the beginning, the two drops are characterised by a different concentration (see the different colours inside the drops, one close to dark blue, the other close to light blue at $t^+ = 295$). However, and differently from the previous case, the

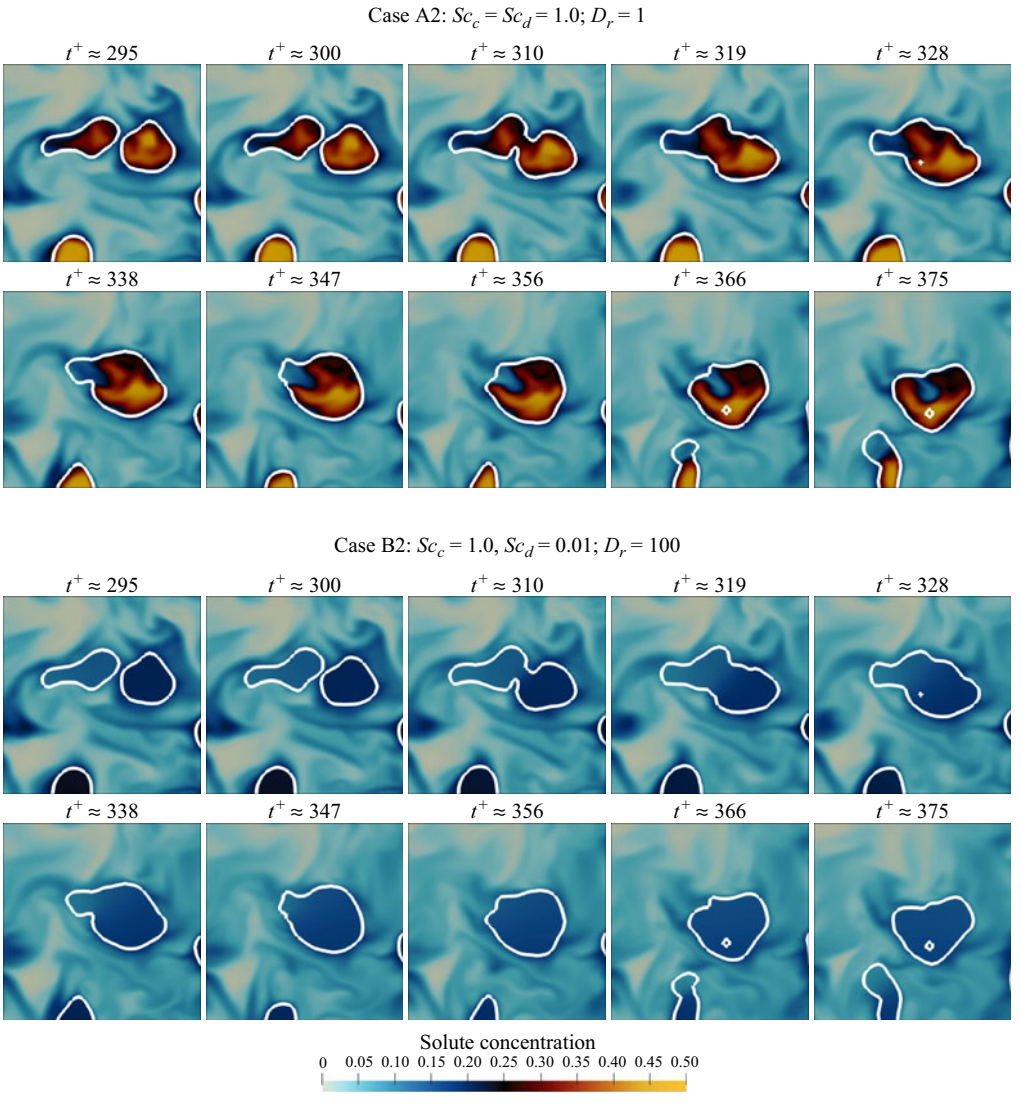

Figure 2. Snapshots separated by $\Delta t^+ = 5$ of a solute concentration field on a horizontal plane ($x-z$) at time sequence $t^+ = (295, 375)$. Influence of the coalescence event on the concentration field inside and outside of the drop for case A2 with Schmidt number of the dispersed phase $Sc_d = 1.0$ (without diffusivity ratio) and case B2 with $Sc_d = 0.01$ (with diffusivity ratio). Both simulations are characterised by a Schmidt number in the carrier flow $Sc_c = 1.0$.

species concentration inside each of the two drops is much more homogeneous. Once the drops have merged, the internal concentrations rapidly homogenise by diffusion (which is the leading transport mechanism in this case, since the time scale of diffusion is much shorter than that of advection) and the concentration gradients inside the newly formed drop are smaller.

Also visible is the fact that the overall efficiency of the species transport mechanism strongly depends on the species diffusivity in the carrier flow (Sc_c) where the drops are immersed: indeed, the bottleneck of the mass-transfer process is represented by the Schmidt number of the carrier flow, with the Schmidt number of the drops playing a relatively less significant – though important – role, as discussed below. This is clearly

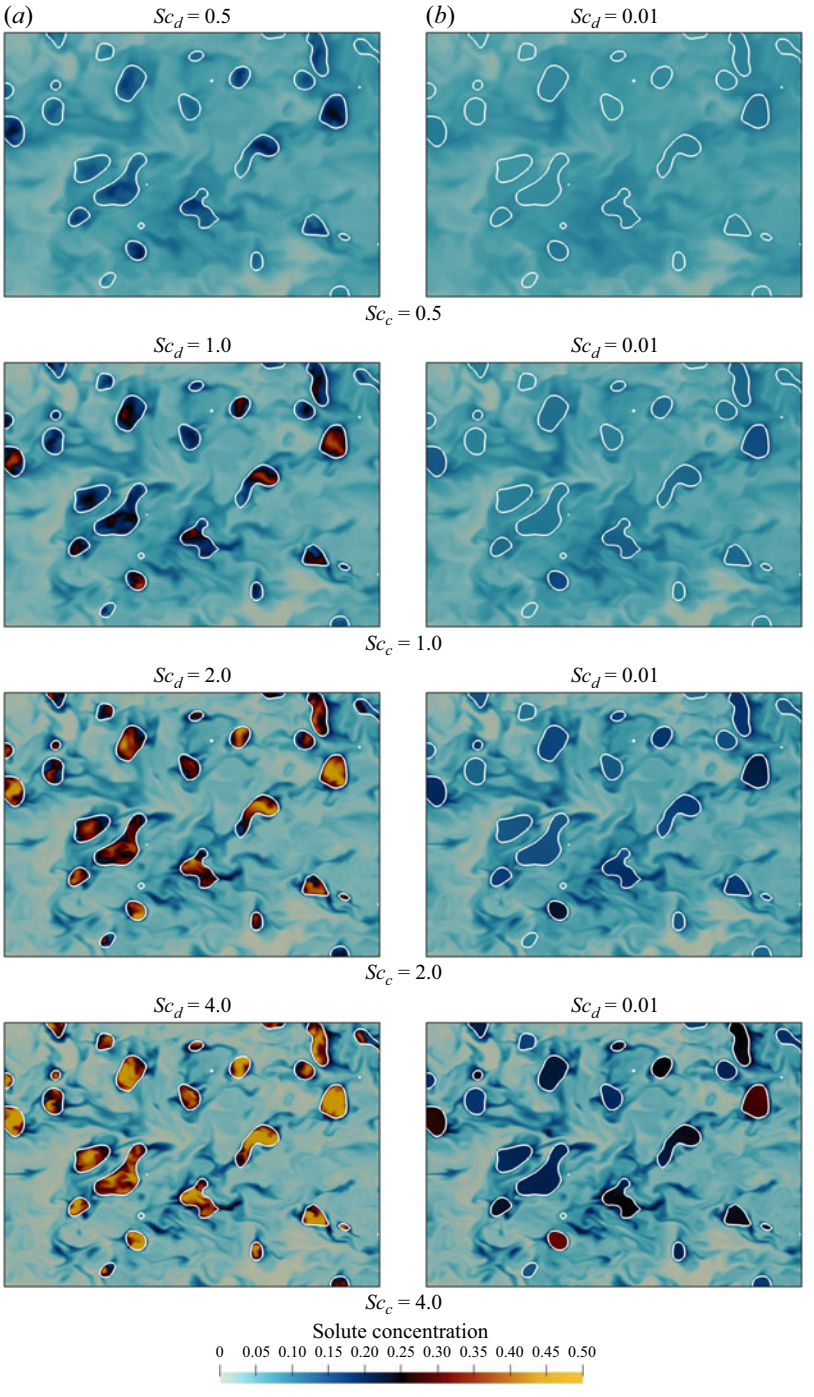

Figure 3. Instantaneous visualisation of the solute concentration field on a portion of a horizontal plane $(x-z)$ of length $\Delta L_x/h = 6.08$ and width $\Delta L_z/h = 4.28$, located at $y/h = 0.5$ at $t^+ = 500$. The interface of the drops (iso-level $\chi = 0.5$) is represented by the white line. Each row refers to a different Schmidt number of the carrier phase: from top to bottom, $Sc_c = 0.5,\ 1.0,\ 2.0,\ 4.0$, respectively. (*a*) Case A. (*b*) Case B.

visualised in figure 3, where the instantaneous distribution (taken at $t^+ = 500$) of the species concentration on a portion of a horizontal plane ($x-z$) of length $\Delta L_x/h = 6.08$ and width $\Delta L_z/h = 4.28$, located at $y/h = 0.5$ (i.e. where drops are initially released), is given for all cases considered in the present study. Each row corresponds to a different Schmidt number of the carrier flow, from $Sc_c = 0.5$ (top) to $Sc_c = 4$ (bottom). The left-hand column refers to simulations in which the Schmidt number of the dispersed phase is equal to the Schmidt number of the carrier flow, $Sc_d = Sc_c$ (simulations A in table 1); the right-hand column refers to simulations in which the Schmidt number of the dispersed phase is kept constant $Sc_d = 0.01$, i.e. large diffusivity inside the drops (simulations B in table 1). As expected, the smaller is Sc_c (i.e. the larger the species diffusivity), the faster is the mass transfer from the dispersed phase to the carrier flow (see the difference between the concentration inside the drops at $Sc_c = 0.5$ – close to blue, top row – and the solute concentration inside the drop at $Sc_c = 4$ – close to red/yellow, bottom row). In addition, while at $Sc_c = 0.5$ the species concentration in the carrier flow is more homogeneous (because the species diffuses more efficiently), at higher Sc_c the species concentration is characterised by sharper gradients and thinner filamentary structures. However, and because of the non-negligible role of the species diffusivity inside the drops, even when the Schmidt number of the carrier phase is the same between two cases (comparison of cases arranged in each row), the species concentration in the carrier phase can be slightly different. This is due to the fact that the concentration inside the drops can change (different Sc_d), and so does the concentration at the interface, thereby inducing a different interfacial flux of species and a different concentration in the carrier flow. We will come back to this point later, when we compare the average mass-transfer flux for cases at the same Sc_c but different Sc_d (see figure 5 and corresponding discussion).

4.1. *Quantitative analysis*

We now characterise the mass-transfer process from a quantitative viewpoint. To begin with, we focus on the average solute concentration in the dispersed phase, $\bar{c}_d$, and in the carrier flow, $\bar{c}_c$, computed as

$$\bar{c}_d = \frac{1}{V_d}\int_{V_d} c\,\mathrm{d}V, \quad \bar{c}_c = \frac{1}{V_c}\int_{V_c} c\,\mathrm{d}V, \tag{4.1}$$

where V_d and V_c are the volume of all drops (considered as an ensemble) and of the carrier flow, respectively. The time evolution of $\bar{c}_d$ and $\bar{c}_c$ is shown by symbols, for all different simulations performed in the present study, in figure 4. In particular, figure 4(*a*) refers to case A simulations (i.e. $Sc_c = S_d$ increasing from 0.5 to 4, and keeping diffusivity ratio $D_r = 1$), while figure 4(*b*) refers to case B simulations (i.e. Sc_c increasing from 0.5 to 4 while $Sc_d = 0.01$, which gives a diffusivity ratio D_r increasing from 50 to 400). Together with the results given by the DNS (symbols), we also provide the prediction obtained by a simplified lumped-parameter model (solid lines), whose detailed description is given in § 5. Starting from the initial condition, at which the species concentration inside the drops is $\bar{c}_d = 1$ – i.e. fully saturated drops – and $\bar{c}_c = 0$ – i.e. carrier flow depleted of species – and regardless of the value of the species diffusivity in both phases (i.e. Sc), $\bar{c}_d$ monotonically decreases and $\bar{c}_c$ monotonically increases, until the equilibrium steady-state condition $\bar{c}_{ss} = \bar{c}_d = \bar{c}_c = 0.054$ is reached. During this transient, mass transfer is progressively reduced until it finally stops. For this reason, we decided to block our simulations at $t^+ = 3000$, a condition at which $(\bar{c}_{ss} - \bar{c}_c)/\bar{c}_{ss} < 2\%$, for all cases. The influence of the Schmidt number of the carrier flow, Sc_c, is apparent: the smaller the value of Sc_c (i.e. the larger the species diffusivity in the carrier flow), the faster the mass-transfer

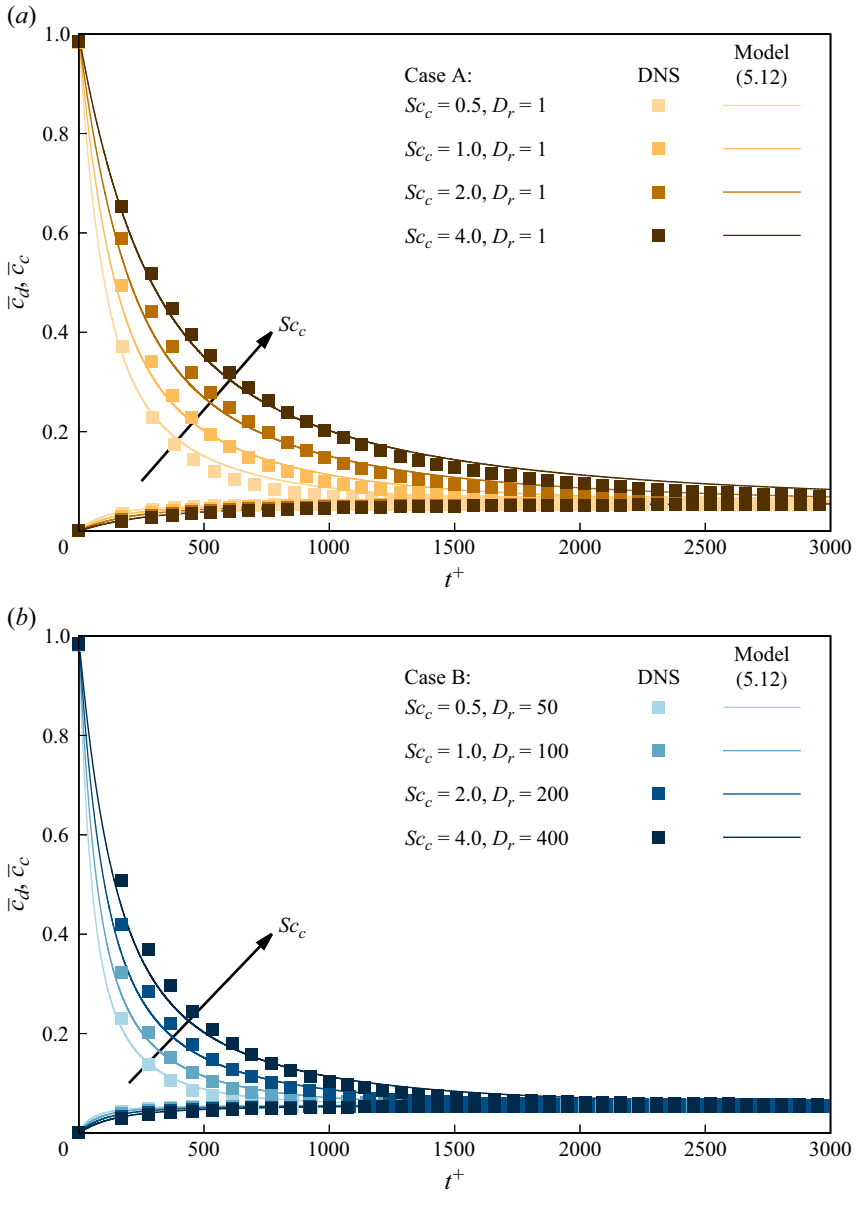

Figure 4. Time evolution of the average species concentration in the drops and in the carrier phase for (*a*) case A (without diffusivity ratio) and (*b*) case B (with diffusivity ratio) simulations, at Schmidt number of the carrier flow $Sc_c = 0.5,\ 1,\ 2,\ 4$. Symbols (filled squares) represent results obtained by DNS, while solid lines represent the predictions obtained by the simplified phenomenological model, (5.12), described in § 5.

process, no matter the value of Sc_d (i.e. similar trends are observed for case A and case B simulations).

Of interest is now to evaluate the evolution of the mass-transfer process considering the same Schmidt number in the carrier flow, but a different Schmidt number in the dispersed phase (i.e comparing one case A with one case B simulation). This comparison cannot be easily done by looking at figure 4, where case A and case B simulations are shown in different panels. Therefore, we decided to make a one-to-one comparison, focusing on

the case $Sc_c = 1$ and plotting simulation A2 ($Sc_d = Sc_c = 1$, i.e. $D_r = 1$) together with simulation B2 ($Sc_d = 0.01$, $Sc_c = 1$, i.e. $D_r = 100$). Results are shown in figure 5 by plotting the derivative in time of the average drop concentration, $\mathrm{d}\bar{c}_d/\mathrm{d}t$ (main panel) as well as the average concentration, c_d and c_c (inset). At the beginning, the species is released more efficiently for case B (higher $\mathrm{d}\bar{c}_d/\mathrm{d}t$, main panel of figure 5*a*) than for case A. This result, which is expected given the larger species diffusivity for case B ($Sc_d = 0.01$), reflects onto a corresponding decrease of c_d that is faster for case B than for case A (inset of figure 5*a*). There is a crossover point between $\mathrm{d}\bar{c}_d/\mathrm{d}t$ for case A2 and B2, after which $\mathrm{d}\bar{c}_d/\mathrm{d}t$ for case A2 becomes greater than $\mathrm{d}\bar{c}_d/\mathrm{d}t$ for case B2, indicating that mass transfer becomes more efficient for case A2 than for case B2.

This is investigated by taking three snapshots – one before the crossover, at $t^+ = 25$ (figure 5*b*), one at the crossover, at $t^+ = 150$ (figure 5*c*), and one after the crossover, at $t^+ = 600$ (figure 5*d*) – of the solute concentration on a plane parallel to the wall and located at $z = h/2$ (plane at which drops are initially released). At the beginning the species concentration is rather uniform for both cases A2 and B2 (see figure 5*b*), and the mass-transfer rate is controlled by the diffusivity inside the drop, giving higher mass-transfer rates (flux of species) for case B2, and therefore lower species concentration inside the drops (see bullet points at $t^+ = 150$ in figure 5*a*). At later stages, the situation is reversed. Mass transfer (flux of species) becomes more efficient for case A, given the relatively larger average species concentration inside the drops.

While case B (with diffusivity ratio $D_r = 100$) exhibits a faster species flux than case A only during the early stages of the process, the overall process reaches a steady-state condition more rapidly (inset of figure 5*a*). This indicates that an increase of the species diffusivity inside the drop (case B, $D_r > 1$) enhances the overall mass-transfer efficiency, thereby resulting in a larger mass-transfer velocity compared with a case with unitary diffusivity ratio (case A, $D_r = 1$).

5. A lumped-parameter model for mass transport in drop-laden flows

The average concentration profiles shown in figure 4 exhibit clear self-similarity. This behaviour can be captured using a simplified phenomenological model for mass transfer in drop-laden turbulent channel flow. Consistent with the assumptions adopted in the DNS, the lumped-parameter model considers identical density and viscosity for the dispersed and carrier phases ($\rho_r = 1$, $\mu_r = 1$) (Mangani *et al.* 2024).

We begin by considering the mass transfer from a drop of diameter d_d^* to the surrounding fluid:

$$\frac{\mathrm{d}N^*}{\mathrm{d}t^*} = \mathcal{K}^* A_d^* \left(c_d^* - c_c^*\right), \tag{5.1}$$

where N^* is the number of moles of a given species, A_d^* is the external surface of the drop, $\mathcal{K}^*$ is the mass transfer coefficient, while c_d^* and c_c^* are the concentrations of the species inside the dispersed phase and in the carrier flow. Note that the asterisk denotes dimensional quantities. In analogy with heat-transfer processes, the mass-transfer coefficient can be estimated as the ratio between the diffusion coefficient (of the carrier flow), D^*, and a reference length scale, here represented by the concentration boundary-layer thickness δ_c^*:

$$\mathcal{K}^* \sim D^*/\delta_c^*. \tag{5.2}$$

In addition, the concentration boundary layer δ_c^* is expressed as $\delta_c^* = \delta^* Sc^{-\beta}$, where δ^* is the momentum boundary-layer thickness and β is an exponent that depends on the

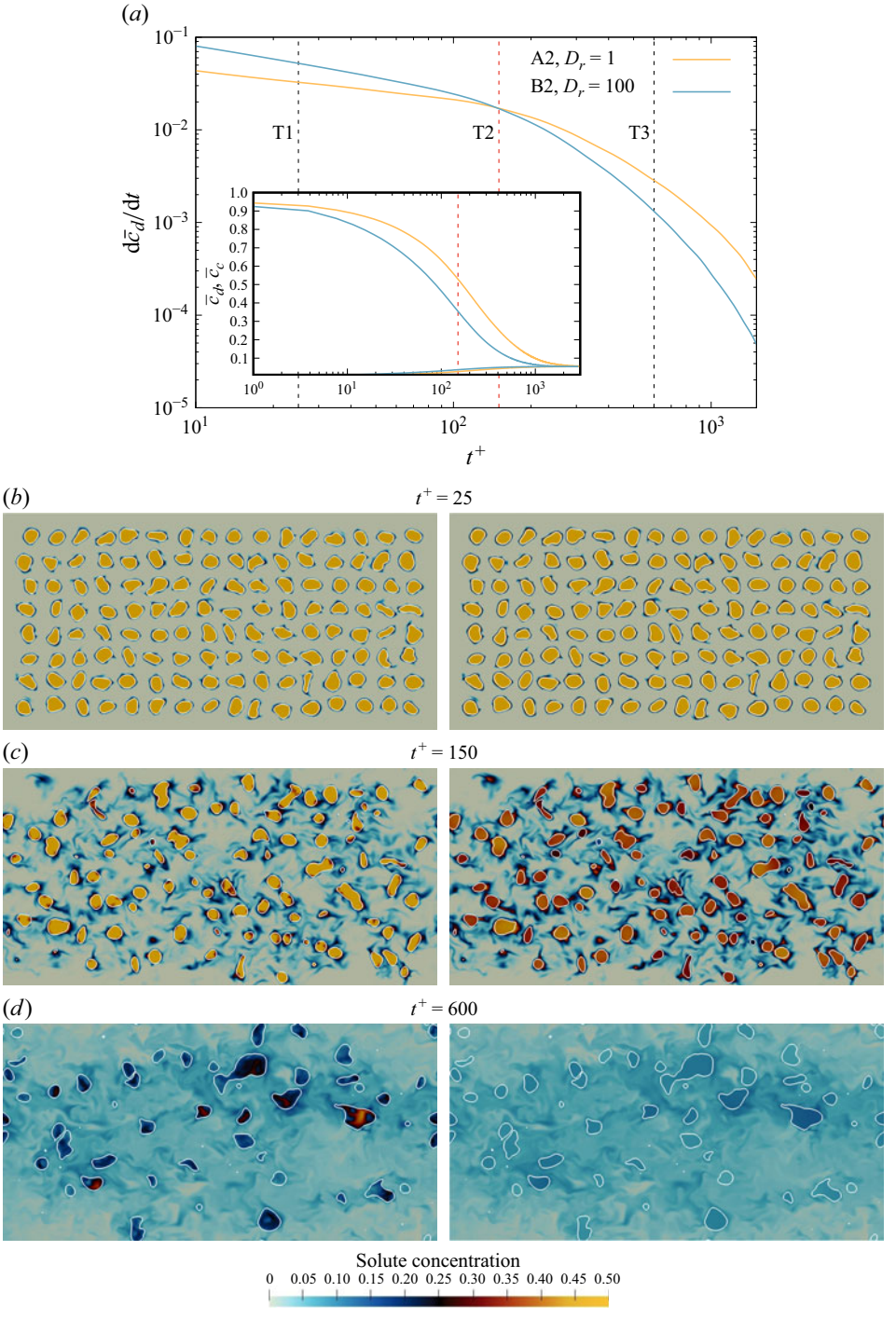

Figure 5. (*a*) Time evolution of the flux of species $\mathrm{d}\overline{c}_d/\mathrm{d}t$ for case A at $D_r = 1$ and case B at $D_r = 100$ and Schmidt number of carrier phase $Sc_c = 1$. In the inset, the behaviour of the average solute concentration in dispersed phase and carrier flow, $\overline{c}_d$, $\overline{c}_c$, is shown as a function of time. (*b–d*) Instantaneous visualisation of the solute concentration field on a horizontal plane (x–z) located at the channel quarter for $t^+ = 25,\ 150,\ 600$.

flow conditions in the near-interface region. Typical values range from $\beta = 1/3$ for no-slip conditions to $\beta = 1/2$, commonly assumed for clean drops or bubbles. In the present study, $\beta = 1/2$ is adopted (see Mangani *et al.* 2024).

With these assumptions, recalling that the concentration of species is $c^* = N^*/V_d^*$, with V_d^* the drop volume, and using the initial drop-to-carrier concentration difference $\Delta c^{*,0} = c_d^{*,0} - c_c^{*,0}$ as the reference concentration (superscript '0' denotes the initial time), h^*/u_b^* as the reference time and h^* as the reference length, (5.1) can be rewritten in dimensionless form as follows:

$$\frac{\mathrm{d}c_d}{\mathrm{d}t} = 6Re_\delta^{-1} Sc^{-1+\beta} \, (d_d)^{-1} \, (c_d - c_c), \tag{5.3}$$

where d_d is the dimensionless drop diameter in outer units, while $Re_\delta = u_b^* \delta^*/\nu^*$ is the Reynolds number based on the boundary-layer thickness (which can be assumed constant among the different cases, since the concentration is here a passive scalar). In the present case, since $\beta = 1/2$ (typical of clean drops/bubbles), we obtain

$$\frac{\mathrm{d}c_d}{\mathrm{d}t} = \mathcal{C} Sc^{-1/2} \, (d_d)^{-1} \, (c_d - c_c), \tag{5.4}$$

where the model parameter $\mathcal{C} = 6Re_\delta^{-1} = 6 \times 10^{-3}$ is evaluated upon comparison of the model results with the current DNS data for the base case of $Sc_c = 1$ and $D_r = 1$ (simulation A2), and then kept for all simulations. It is worth mentioning that $\mathcal{C}$ could change depending on the flow Reynolds number and/or the flow configuration. Now we extend the model considering that the concentration in the interior of the drop is not always uniform (as it would be in the case of perfectly mixed substances). If a concentration boundary layer exists also inside the drop, the mass-transfer process can be regarded as a two-step process: the mass transfer from the core of the drop to its interface (inner region labelled 'i', characterised by an inner mass-transfer coefficient, $\mathcal{K}_i^*$); and the mass transfer from the interface to the surrounding fluid (outer region labelled 'o', characterised by an outer mass-transfer coefficient, $\mathcal{K}_o^*$). With the constraint of the continuity of the molar flux at the interface,

$$\mathcal{K}_i^* A_d^* \left(c_d^* - c_{d,i}^*\right) = \mathcal{K}_o^* A_d^* \left(c_{d,o}^* - c_c^*\right), \tag{5.5}$$

recalling that $\mathcal{K}_o^* \propto D_o^*/\delta_o^*$ and $\mathcal{K}_i^* \propto D_i^*/\delta_i^*$, and assuming that the kinematic viscosity is uniform, $\nu_i^* = \nu_o^* = \nu^*$, and that the boundary-layer thickness inside and outside of the drop does not change, $\delta_o = \delta_i$, we finally get

$$c_{d,i} = \frac{c_d Sc_o + c_c Sc_i}{\alpha Sc_i + Sc_o}, \tag{5.6}$$

where Sc_i and Sc_o are the values of the Schmidt number inside and outside of the drop. Unlike the heat-transfer case, for mass transfer there can be a jump of concentration at the drop interface, $c_{d,o} = \alpha c_{d,i}$, therefore giving

$$\frac{\mathrm{d}c_d}{\mathrm{d}t} = \mathcal{C} Sc_o^{-1/2} \, (d_d)^{-1} \left(c_{d,o} - c_c\right) = \mathcal{C} Sc_o^{-1/2} \, (d_d)^{-1} \left(\alpha c_{d,i} - c_c\right), \tag{5.7}$$

with $c_{d,i}$ given by (5.6). Note that in the present study we always have $\alpha = 1$, i.e. continuity of the concentration at the drop interface. Considering now that the turbulent flow is laden with drops of different diameters, the equation that describes the mass transfer from the jth drop of given diameter $d_{d,k}$ (with k indicating the kth diameter) becomes

$$\frac{\mathrm{d}c_{d,j}}{\mathrm{d}t} = \mathcal{C} Sc_o^{-1/2} \left(d_{d,k}\right)^{-1} \left(c_{d,i,j} - c_c\right) = \mathcal{F}_j, \tag{5.8}$$

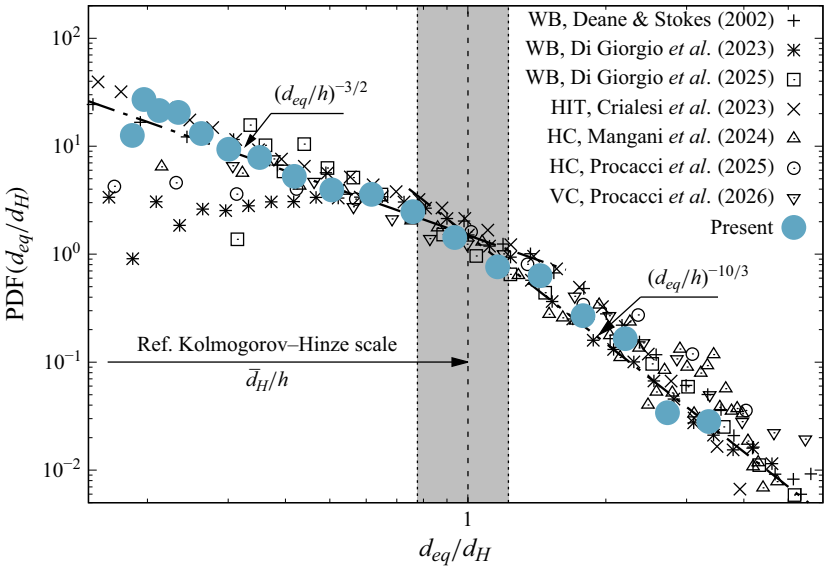

Figure 6. Steady-state size distribution of the drops. The Kolmogorov–Hinze scale is shown as the shaded area, computed using the values of the turbulent kinetic energy dissipation rate ϵ at $y/h = 0.5$ and $y/h = 1$. The reference Kolmogorov–Hinze scale, corresponding to the midpoint between these two limits, is indicated by the vertical dashed line. The two scaling laws, $(d_{eq}/h)^{-3/2}$ for the coalescence-dominated regime (small drops) and $(d_{eq}/h)^{-10/3}$ for the breakage-dominated regime (larger drops), are represented by the dash-dotted lines. In addition, datasets from several available literature studies are also reported: experimental wave breaking (Deane & Stokes 2002), numerical wave breaking (Di Giorgio *et al.* 2022, 2025), numerical homogeneous isotropic turbulence (Crialesi-Esposito, Chibbaro & Brandt 2023), numerical horizontal drop-laden channel (Mangani *et al.* 2024; Procacci *et al.* 2025) and vertical bubble-laden channel (Procacci *et al.* 2026).

where $\mathcal{F}_j$ is a lumped-parameter representation of the rate of change of concentration for the jth drop. To make the model self-contained, we assume that the distribution of drops follows a predefined equilibrium size distribution (DSD), in which the number density of drops scales as ${d_d}^{-3/2}$ in the sub-Hinze-scale range, and as ${d_d}^{-10/3}$ in the super-Hinze-scale range. The value of the Hinze scale, $d_H = 0.725(\rho/\sigma)^{-3/5}|\epsilon|^{-2/5}$, with ϵ the turbulent kinetic energy dissipation, is expected to vary in the range $0.21 < d_H < 0.41$ (see shaded area in figure 6), and corresponding to ϵ evaluated at $y/h = 1/2$, where the drops are initially released, or at the channel centre, $y/h = 1$, where drops preferentially migrate. This type of distribution has been observed in the literature (Deane & Stokes 2002; Roccon *et al.* 2023), and is also confirmed in this study (see figure 6). To approximate the distribution shown in figure 6, we use 12 classes of drop diameter in the sub-Hinze range ($0.035 < d/h < 0.35$), and 4 classes in the super-Hinze range ($0.35 < d/h < 0.6$). The choice of the minimum drop size, the maximum drop size and the Hinze drop size depends on the application, and should be evaluated according to experiments, DNS (as done in the present case) or other literature data/predictions. Equation (5.8) can be integrated in time to give

$$c_{d,j}^{n+1} = c_{d,j}^{n} + \Delta t \mathcal{F}_j^n, \tag{5.9}$$

and, weighting by the number of drops in each of the k classes (as per DSD), we obtain the average drop concentration, $\bar{c}_d$, at each time instant. The mean concentration of the carrier flow is obtained considering that the mass released by the drops is absorbed by the carrier flow. The mass released by the drops of a certain class (i.e. certain diameter d_d for a class

k, $d_{d,k}$) is

$$\mathcal{M}_k^n = V_d \mathcal{F}_j^n \mathcal{N}_{d,k}, \tag{5.10}$$

where $\mathcal{N}_{d,k}$ is the number of drops for that specific class k (as per DSD) and V_d the corresponding drop volume. The overall mass released by all drops can be calculated as the summation over all classes:

$$\mathcal{M}_{tot}^n = \sum_{k=1}^{\mathcal{N}_c} \mathcal{M}_k^n, \tag{5.11}$$

where $\mathcal{N}_c$ is the employed number of classes. We finally get the mean concentration of species in the carrier flow as

$$\overline{c}_c^{n+1} = \overline{c}_c^n + \Delta t \left(-\mathcal{M}_{tot}^n / V_c\right), \tag{5.12}$$

with V_c the volume of the carrier flow (obtained from the volume fraction ϕ). The results of the model for the averaged species concentration inside the drops and in the carrier flow are shown in figure 4 (solid lines). As initial condition ($n = 0$) to solve (5.9) and (5.12), we use the same initial condition used in the DNS simulations, i.e. $\overline{c}_d^0 = 1$ and $\overline{c}_c^0 = 0$. Despite the many simplifications introduced to derive the model (chiefly, spherical shape of the drops, stationary drop-size distribution evaluated at the equilibrium, zero-dimensional model), we observe that the behaviour of the mean concentration is captured fairly well by the model (comparison between symbols and corresponding solid line), for almost all cases (which indeed cover a range of different physical situations).

5.1. *Scaling of mass-transfer rate with Schmidt number*

A key parameter in mass-transfer processes is the mass-transfer rate (or velocity), $\mathcal{K}$. In particular, as mentioned in § 5, and in view of developing more reliable, flexible and accurate models, it is crucial to evaluate the behaviour of $\mathcal{K}$ as a function of the diffusivity of the working fluids (i.e. their Schmidt number, Sc). For mass transfer at a deformable interface, the seminal works of Boussinesq (1905) and Levich (1962) have shown that

$$\mathcal{K} \propto Sc^{-n}, \tag{5.13}$$

with $n = 1/2$. This scaling was also confirmed by numerical simulations, run in controlled settings, of isolated non-interacting bubbles immersed in an isotropic turbulent flow (Clift, Grace & Weber 2005; Farsoiya *et al.* 2021). In different scenarios, such as air–sea interfaces with flat and wavy surfaces, the exponent n in (5.13) is expected to vary between $n \approx 1/2$ and $n \approx 2/3$ (Hanratty 1991; Jähne & Haußecker 1998; Wanninkhof *et al.* 2009). We are now ready to use our DNS database to compute the mass-transfer rate. Because of its robustness, ease of implementation and usefulness in view of comparing results from simulations and experiments, we evaluate the mass-transfer rates following the approach suggested by Colombet *et al.* (2015). The evolution in time of the solute concentration within the drops can be written as (Colombet *et al.* 2015)

$$\frac{\mathrm{d}\overline{c}_d}{\mathrm{d}t} = \mathcal{K} a_0 \left(\alpha \overline{c}_d - \overline{c}_c\right), \tag{5.14}$$

where $a_0 = A_0 / V_0$, with A_0 the total initial interface area between dispersed phase and carrier flow and V_0 the total volume of the domain. Equation (5.14) can be rewritten as

$$\frac{\mathrm{d}\overline{c}_d}{\mathrm{d}t} = (1/\tau) \left(\alpha \overline{c}_d - \overline{c}_c\right), \tag{5.15}$$

Type of study	Type of configuration		$\mathcal{K}_{Sc1}$
Numerical	Case A (see table 1)	Present	0.0117
	Case B (see table 1)	—	0.0209
	Case A model (5.12)	—	0.0098
	Case B model (5.12)	—	0.0195
Numerical	Flat, wind-wave	Takagaki *et al.* (2016)	0.0932
	Flat	Calmet & Magnaudet (1998)	0.0932
	Flat	Hasegawa & Kasagi (2003; 2006; 2008)	0.0932
	Wind-wave	Komori *et al.* (2010)	0.0932
	Wind-wave	Takagaki *et al.* (2015)	0.0932
	Bubble	Farsoiya *et al.* (2021)	10.606
	—	—	16.370
	—	—	22.627
Experimental	Waves/flat	Jähne & Haußecker (1998)	—
	Wind-wave	Jähne *et al.* (1987)	0.0932
	Wind-wave	Iwano *et al.* (2012; 2013)	0.0932
Experimental/numerical	Flat	Herlina & Wissink (2019)	0.576

Table 2. Summary of available numerical and experimental data plotted in figure 7. In particular, we report the type of study (numerical or experimental), the type of configuration (numerical/experimental set-up), a reference to the corresponding available studies and the values of $\mathcal{K}_{Sc1}$ used to normalise the data and to obtain $\mathcal{K}^+ = \mathcal{K}/\mathcal{K}_{Sc1}$.

where τ is the time constant of the system, which can be evaluated as the time taken by the drop concentration to reach a given threshold value. As mentioned, this setting for the definition of the mass-transfer rate is particularly useful also in the experimental context, where the calculation of the local heat-transfer fluxes at the drop interface are almost never accessible. In experiments, the time constant can be evaluated as the time taken by the signal recorded by a specific probe to trespass a given threshold value for the species concentration. The mass-transfer rate coefficient is then evaluated as

$$\mathcal{K} = \frac{1}{a_0 \tau}. \tag{5.16}$$

Sometimes, and in particular in the context of industrial applications, the Sherwood number Sh, i.e. the total to the diffusive mass-transfer ratio, is introduced. In the present case,

$$Sh = \mathcal{K} \frac{Sc_c Re}{u_b}. \tag{5.17}$$

Current results of $\mathcal{K}$ as a function of Sc, obtained from (5.16), and estimating τ as the time taken by the average concentration within the drops to become $\overline{c}_d = 0.1$ (i.e. lost of 90 % of the initial solute concentration), are shown in figure 7. To compare our results with available literature data, and to infer about possible scaling laws of type $\mathcal{K} \sim Sc^n$, it is convenient to normalise the value of $\mathcal{K}$ with respect to the reference value obtained at $Sc = 1$, $\mathcal{K}_{Sc1}$. Given the available literature data, we choose to normalise the numerical and experimental results for the flat and wind-wave scenarios using the $\mathcal{K}_{Sc1}$ value at $Sc = 1$ obtained by Takagaki *et al.* (2016). In contrast, the data from Herlina & Wissink (2019) and Farsoiya *et al.* (2021) are normalised using the reference values provided by the respective authors. All details, along with the reference values $\mathcal{K}_{Sc1}$ used to normalise the data, are listed in table 2.

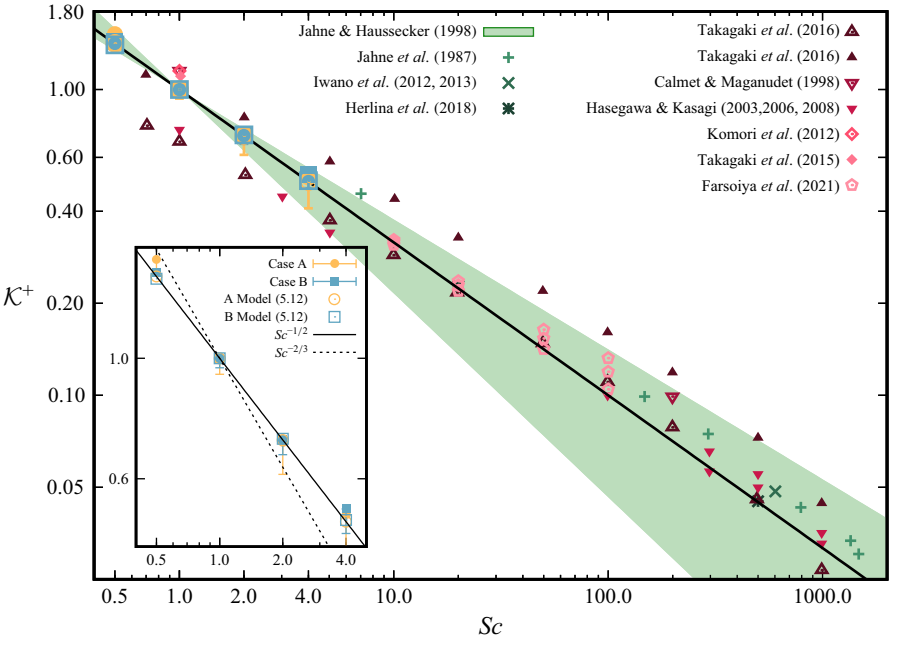

Figure 7. Behaviour of the normalised gas-transfer velocity, $\mathcal{K}^+$, as a function of the Schmidt number Sc: filled symbols represent current results with diffusivity ratio $D_r = 1$, i.e. case A (filled circles) and with diffusivity ratio $50 < D_r < 400$, i.e. case B (filled squares). Open symbols refer to simplified model (see § 5, (5.12)). In addition, datasets from several available literature studies are also reported: experimental data of wind-driven wavy interface (Jähne *et al.* 1987; Jähne & Haußecker 1998; Iwano *et al.* 2012, 2013), numerical results for both wavy and flat interfaces (Calmet & Magnaudet 1998; Hasegawa & Kasagi 2003, 2006, 2008; Komori *et al.* 2010; Takagaki *et al.* 2015, 2016), numerical and experimental results for flat surfaces (Herlina & Wissink 2019) and numerical simulations of a single bubble in isotropic turbulence (Farsoiya *et al.* 2021). Note that, to facilitate comparison among the different datasets (different configurations, both numerical and experimental), $\mathcal{K}^+ = \mathcal{K}/\mathcal{K}_{Sc1}$ is normalised by the corresponding value at $Sc = 1$.

Figure 7 also presents the scaling laws proposed in the literature, and derived from both experimental and numerical data collected under different flow configurations. The scaling range observed by Jähne & Haußecker (1998), highlighted with a green shadow, is based on a series of experimental data (Liss 1973; Broecker, Petermann & Siems 1978; Merlivat & Memery 1983; Jähne *et al.* 1985). In addition, we have also included experimental measurements of mass-transfer rates for a wind-driven wavy interface (Jähne *et al.* 1987; Iwano *et al.* 2012, 2013), as well as numerical results for both wavy and flat interfaces (Calmet & Magnaudet 1998; Hasegawa & Kasagi 2003, 2006, 2008; Komori *et al.* 2010; Takagaki *et al.* 2015), numerical and experimental results for flat surfaces (Herlina & Wissink 2019) and results of numerical simulations of a bubble immersed in isotropic turbulence (Farsoiya *et al.* 2021). The inset of figure 7 highlights the data obtained by our DNS, together with the prediction of the model described in § 5 (open circles and squares) and the theoretical $Sc^{-2/3}$ and $Sc^{-1/2}$ scalings (Boussinesq 1905; Levich 1962; Hanratty 1991).

As expected, the mass-transfer rate decreases as the Schmidt number increases. This trend is consistent with our previous observations on the behaviour of solute concentration over time (see figure 4). Interestingly, the mass-transfer rate does depend not only on the chemical properties of the transported species, but also on the features of the flow through which the species is transported, including turbulence intensity and interface topology.

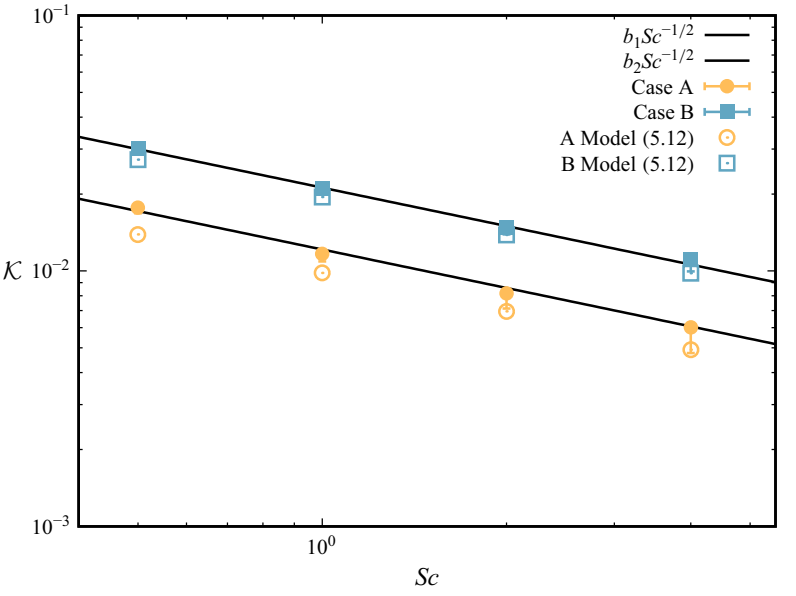

Figure 8. Behaviour of the gas-transfer velocity, $\mathcal{K}$, as a function of the Schmidt number Sc: filled symbols represent current results with diffusivity ratio $D_r = 1$, i.e. case A (filled circles) and with diffusivity ratio $50 < D_r < 400$, i.e. case B (filled squares). Open symbols refer to simplified model (see § 5, (5.12)) The solid lines correspond the law $\mathcal{K} = b_{1,2} Sc^{-1/2}$, where $b_1 = 0.012$ and $b_2 = 0.021$.

Different flow conditions can lead to different scaling behaviours: for example, in the presence of a smooth interface, the scaling of the mass transfer through the interface is close to $Sc^{-2/3}$, while in a wind-driven configuration it tends to $Sc^{-1/2}$ (Hanratty 1991). Similarly for a single bubble in isotropic turbulence (Farsoiya *et al.* 2021).

The comparison of our DNS results, which consider the case of mass transfer in drop-laden turbulence, with literature results covering a broad spectrum of scenarios (i.e. gas–liquid systems, wave breaking, bubble-laden turbulence) yields an interesting consideration: for both $D_r = 1$ and $D_r > 1$ our results consistently exhibit the scaling $\mathcal{K} \propto Sc^{-1/2}$, in line with most of the previous literature predictions. This agreement seems to indicate the universal nature of the mass-transfer process, at both liquid–liquid and gas–liquid interfaces, no matter the specific flow configuration. We remark that, while the DSD evolves from the initial monodisperse to a near-equilibrium DSD state, most of the mass-transfer process occurs with the near-equilibrium DSD, ensuring that the current results are representative of physically relevant conditions. Note that these findings have direct implications also on experimental studies. Because experiments often rely on the use of different tracers to estimate the transport properties of the flow, understanding how the Schmidt number of a tracer influences mass transfer across various flow regimes is crucial to offer a fair interpretation of the results and a reliable extrapolation of predictions to environmental and industrial applications. Note that, since $Sh \sim Sc^n$, $\mathcal{K} \sim Sc^{n-1}$.

While the normalised value $\mathcal{K}^+ = \mathcal{K}/\mathcal{K}_{Sc1}$ is useful to compare results obtained under very different conditions and to infer possible universal scaling laws, it is now interesting to turn our attention to the actual mass-transfer velocity $\mathcal{K}$ (i.e. not normalised by $\mathcal{K}_{Sc1}$). This is shown in figure 8. As expected, results can be conveniently parametrised as $\mathcal{K} = bSc^{-1/2}$. However, the value of the prefactor b does depend on the specific case considered: $b = 0.012$ for $D_r = 1$ (case A), while $b = 0.021$ for $D_r > 1$ (case B). This highlight the enhanced efficiency of the mass-transfer process when the mass diffusivity

inside the drop is larger than outside of the drop. In particular, the ratio between the mass-transfer velocity is $\mathcal{K}_{D_r>1}/\mathcal{K}_{D_r=1} \simeq 1.75$. We note that grid convergence tests performed on a reduced domain (Appendix A.3) indicate uncertainties of approximately 10 %–20 % in the predicted mass-transfer velocity at the highest Schmidt number considered ($Sc = 4$). While the qualitative scaling $\mathcal{K} \propto Sc^{-1/2}$ is robust across all grid resolutions tested, quantitative predictions at high Sc should be interpreted with this level of uncertainty in mind. This results is in agreement with the two-film model of Liss & Slater (1974), in which the total resistance to the mass transfer is the sum of the resistance in either phase, leading to a mass-transfer velocity $\mathcal{K}$ (Wanninkhof *et al.* 2009):

$$\frac{1}{\mathcal{K}} = \frac{1}{\mathcal{K}_d} + \frac{1}{\mathcal{K}_c}, \tag{5.18}$$

with $\mathcal{K}_d$ and $\mathcal{K}_c$ the mass-transfer velocities through the diffusive sublayers in the dispersed-phase side and carrier-phase side of the interface, respectively. Since $\mathcal{K} \propto Sc^{1/2}$, we have $1/\mathcal{K} \propto \sqrt{Sc_d} + \sqrt{Sc_c}$, thereby giving $\mathcal{K}_{D_r>1}/\mathcal{K}_{D_r=1} = (1.751, 1.818, 1.886, 1.904)$, in agreement with the results found with the DNS.

6. Conclusions

In this work, we have used a combined DNS–VOF approach to study the mass-transfer process in a wall-bounded turbulent channel flow. All drops are initially fully saturated with a given chemical species (i.e. initial species concentration $c_d = 1$), and are injected into the turbulent channel flow, where the chemical species is initially absent (i.e. initial species concentration $c_c = 0$). Because of the given set-up, a net mass transfer (flux of chemical species) from the drops to the carrier flow is established. Three main physical parameters control the process: the Schmidt number Sc (momentum to mass diffusivity ratio), the bulk Reynolds number Re_b (inertia to viscous forces ratio) and the Weber number We (inertia to surface tension forces ratio). In the present study, we kept Re and We constant and equal to $Re_b = 10\,000$ and $We = 3100$, and we varied Sc. Two different sets of numerical simulations have been performed, labelled case A and case B, respectively. In case A simulations, the Schmidt number in the carrier flow, Sc_c, is varied between $Sc_c = 0.5$ and $Sc_c = 4$, and is set to be equal to the Schmidt number inside the drops, $Sc_d = Sc_c$, finally giving a diffusivity ratio $D_r = Sc_c/Sc_d = 1$. In case B simulations, the Schmidt number in the carrier flow is varied between $Sc_c = 0.5$ and $Sc_c = 4$, while the Schmidt number inside the drops is kept constant, $Sc_d = 0.01$, so that the diffusivity ratio is systematically increased between $D_r = 50$ and $D_r = 400$. We analysed the behaviour of the average species concentration inside the drops, $\overline{c}_d$, and inside the carrier flow, $\overline{c}_c$, and we showed that $\overline{c}_d$ decreases in time, while $\overline{c}_c$ increases in time, until reaching an equilibrium condition $\overline{c}_d \simeq \overline{c}_c$. We also showed that fairly accurate predictions of the time behaviour of the concentration profiles can be obtained by a simplified lumped-parameter model. In addition, we focused on the behaviour of the mass-transfer velocity $\mathcal{K}$, which quantifies the rate at which mass is transferred across the interface. Our results consistently showed that $\mathcal{K} \propto Sc^{-1/2}$ for both case A simulations (i.e. when $D_r = 1$) and case B simulations (i.e. when $D_r > 1$), in good agreement with previous literature results covering a broad spectrum of scenarios (gas–liquid and liquid–liquid). These findings seem to highlight the universal nature of the mass-transfer process through deformable interfaces, no matter the specific flow configuration. While the scaling of the mass-transfer velocity with Sc is robust and does not depend on the diffusivity ratio D_r, following the law $\mathcal{K} \propto Sc^{-1/2}$, the magnitude of the mass-transfer velocity does depends on the diffusivity

ratio. In particular, we found that $\mathcal{K}_{D_r>1}/\mathcal{K}_{D_r=1} \simeq 1.75$, a result that highlights the key role of the diffusivity ratio in enhancing the mass-transfer velocity.

Such insights could be critical for the design of more efficient systems in applications where liquid–liquid interactions are pivotal, potentially influencing operational strategies in chemical processing, waste treatment and other industrial applications. Furthermore, the implications of these findings can extend into environmental/geophysical fields. Understanding the drop-mediated gas exchange at the ocean surface, as a function of the diffusivity ratio, can enhance the future ability to model and predict the behaviour of gases in natural water bodies and the atmosphere. This is particularly relevant in studying the transport and fate of greenhouse gases and pollutants, providing crucial data that can inform environmental policy and strategies to mitigate climate change.

Acknowledgements. The results reported in this paper have been achieved using the EuroHPC Research Infrastructure resource LEONARDO based at CINECA, Casalecchio di Reno, Italy, under project EuroHPC R0387.

Funding. The authors gratefully acknowledge financial support from European Union-NextGenerationEU PNRR M4.C2.1.1-PRIN 2022, 'The fluid dynamics of interfaces: mesoscale models for bubbles, drops, and membranes and their coupling to large scale flows' 2022R9B2MW-G53C24000810001.

Declaration of interests. The authors report no conflict of interest.

Appendix A. Validation

In this appendix we validate our numerical set-up for the case of diffusion from a static and from a rising bubble.

A.1. *Diffusion from a static bubble*

Following previous works (see e.g. Farsoiya *et al.* 2021), we benchmark our numerical implementation considering the diffusion from a stationary spherical bubble of constant size. Consider a stationary, axisymmetric bubble with radius $R_0 = d_0/2$. Let D_g and D_l denote the diffusivities in the gas and liquid phases, respectively. The one-dimensional transient concentration diffusion in spherical coordinates, both inside and outside the bubble, is described by

$$c_b(t, r) = -\frac{2c_{g0}}{\pi r}\int_0^\infty \frac{1}{x}\,\mathrm{Im}\left\{\frac{\sinh\left[\lambda_g(-x)\,r\right]}{\zeta(-x)}\right\}\mathrm{e}^{-xt}\,\mathrm{d}x, \tag{A1}$$

$$c_l(t, r) = \frac{c_{g0}}{\pi r}\int_0^\infty \frac{1}{x}\,\mathrm{Im}\left\{\frac{\xi(-x)}{\zeta(-x)}\mathrm{e}^{-\lambda_l(-x)\,r}\right\}\mathrm{e}^{-xt}\,\mathrm{d}x, \tag{A2}$$

where $\mathrm{Im}(\cdot)$ denotes the imaginary part of a complex number. The derivation of these equations can be found in Farsoiya *et al.* (2021). Together with the analytical predictions, here we also present our numerical solutions for the transient species concentration both inside and outside of the spherical bubble. Note that solute concentrations are expressed as integrals, and are evaluated numerically. For this test, we consider a static bubble with a diameter of $d_0/L = 0.2$, a diffusivity ratio of $D_g/D_l = 10$ and a solubility $\alpha = 10^{-3}$. Figures 9(*a*) and 9(*b*) show the transient concentrations inside the bubble at $r/d_0 = 0.25$ and outside the bubble at $r/d_0 = 0.75$, respectively. Together with the analytical solution (solid line), we also show our numerical predictions for different grid resolutions (coloured symbols). Convergence to the analytical prediction is clearly assessed. To highlight the prediction error of gas exchange through static bubbles, figure 9(*c*) shows the solute concentration error ($\epsilon(c_l)$), defined as the difference between the predicted solute

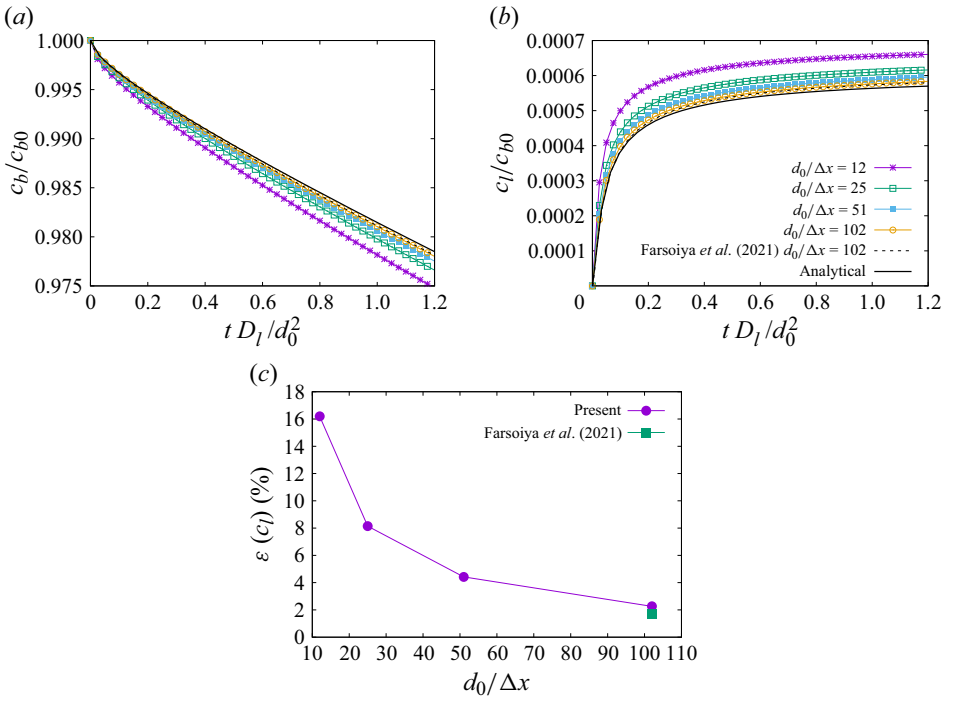

Figure 9. Diffusion from a static bubble, comparing the numerical results with analytical trend and simulation by Farsoiya *et al.* (2021). (*a*) Concentration inside the bubble at $r/d_0 = 0.25$. (*b*) Concentration outside the bubble at $r/d_0 = 0.75$. (*c*) Error (ϵ) (i.e. difference between numerical and analytical predictions) of the concentration outside of the bubble.

concentration outside the bubbles at a fixed time and the analytical solution, as a function of the number of grid points per bubble diameter.

A.2. *Diffusion from a rising bubble*

To further assess our numerical method, and in particular to validate the advection–diffusion scheme, we examine the case of mass diffusion from a bubble rising (under the influence of buoyancy) in a quiescent fluid. The computational set-up (and in particular the values of the Bond and Archimedes, or Morton, numbers) is prepared in accordance with previous literature studies (Darmana, Deen & Kuipers 2006; Roghair 2012; Deising, Marschall & Bothe 2016; Jia, Xiao & Kang 2019; Farsoiya *et al.* 2021). The bubble rise velocity in a still liquid depends on the fluid and bubble properties, i.e. on the Archimedes number $Ar = g d_0^3 \rho_l (\rho_l - \rho_g) \mu_l^2$, the Morton number $Mo = g\mu_l^4/(\rho_l \gamma^3 \sigma)$ and the Bond number $Bo = \rho_l g d_0^2 \sigma$ (Moore 1965; Maxworthy *et al.* 1996; Clift *et al.* 2005; Cano-Lozano *et al.* 2016), and can be expressed via the non-dimensional bubble Reynolds number $Re = \rho_l U d_0/\mu_l$ (Moore 1965; Clift *et al.* 2005). We evaluate two different configurations, corresponding to $Re = 5.6$ and $Re = 32.9$, with Bond numbers $Bo = 1$ and $Bo = 40$, and Archimedes numbers $Ar = 100$ and $Ar = 8000$. We follow Deike, Melville & Popinet (2016) and we compute the mass transfer at Schmidt number $Sc = \mu_l/D_l = 1$ and gas solubility $\alpha = 1/30$. The mass-transfer rate $\mathcal{K}$ is determined as

$$\mathcal{K} = \frac{\mathrm{d}c_g/\mathrm{d}t}{A_g\left(\alpha \bar{c}_g - \bar{c}_l\right)}, \tag{A3}$$

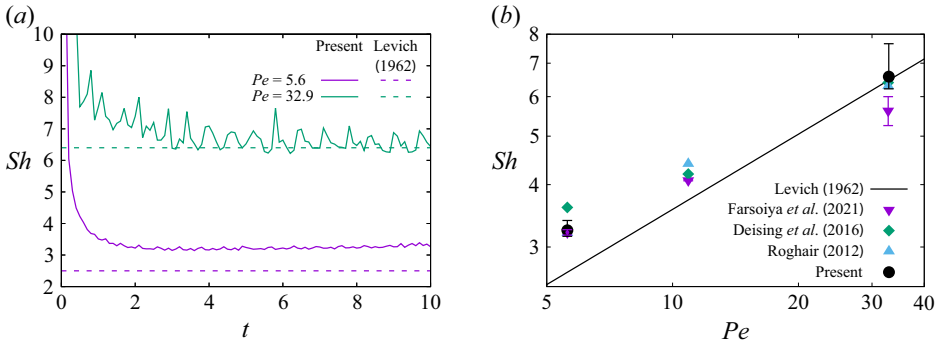

Figure 10. Diffusion from a rising bubble, comparing the numerical results with analytical trend and simulation by Roghair (2012), Deising et al. (2018) and Farsoiya *et al.* 2021). (*a*) Evolution with time of non-dimensional transfer rates, with Levich (1962) predicted values (dashed lines). (*b*) Steady-state transfer rate as a function of Péclet number compared against Levich (1962).

where A_g is the instantaneous surface area of the bubble. Note that the solute concentration inside and outside the bubble is calculated as $c_g = \bar{c}_g V_g$ and $c_l = \bar{c}_l V_l$, where $\bar{c}_g$ and $\bar{c}_l$ are defined in (4.1), and V_g and V_l represent the bubble and liquid volumes, respectively. Simulations are conducted using symmetric boundary conditions, modelling only one-quarter of the bubble, with a resolution of $d_0/\Delta x = 25.6$. The results, shown in figure 10, are benchmarked against previous works. Figure 10(*a*) illustrates the time evolution of the non-dimensional transfer rate, $Sh = \mathcal{K} d_0/D_l$, for both cases, with the mean steady-state values indicated by dashed lines. Figure 10(*b*) compares the values of Sh obtained by current computations with previous literature results. The theoretical prediction $Sh = 2/\sqrt{\pi}\,Pe$ proposed by Levich (1962) is also shown for comparison purposes. Our findings demonstrate that the proposed method produces results consistent with previous studies and aligns well with theoretical predictions.

A.3. *Grid sensitivity analysis*

As a further benchmark, we performed a grid sensitivity analysis on a turbulent flow case. In particular, we performed a series of simulations of a turbulent channel flow with the injection of drops that are initially fully saturated with a given chemical species. This set-up is similar to the one used to run the simulations presented in the main body of this paper. However, in this case, the channel dimensions are $L_x \times L_y \times L_z = \pi h \times 2h \times \pi/2h$, i.e. four times smaller than the full channel discussed in the main body of the paper. Even for the present test, we run case A and case B simulations (i.e. case A with unitary diffusivity ratio $D_r = 1$ and case B with $D_r \gg 1$). We employed three different grid resolutions: coarse ($144 \times 144 \times 72$), medium ($288 \times 288 \times 144$) and fine ($576 \times 576 \times 288$), which correspond, respectively, to half, identical and double resolution compared with the full-channel simulations analysed in the main body of the paper. In these test cases, we considered five different Schmidt numbers of the carrier phase: $Sc_c = 0.5,\ 1,\ 2,\ 4,\ 8$.

Figure 11 shows the mass-transfer velocity $\mathcal{K}$ as a function of Schmidt number (figure 11*a*) and the relative error ϵ in the mass-transfer velocity with respect to the finest grid (figure 11*b*). This test also includes $Sc = 8$, which was not analysed in the full-channel simulations. We observe that the scaling law $\mathcal{K} \propto Sc^{-1/2}$ is predicted fairly well by both medium and fine grid resolutions, while the coarse grid resolution fails to reproduce it accurately for Schmidt numbers $Sc > 2$. The absolute error in mass-transfer velocity ϵ

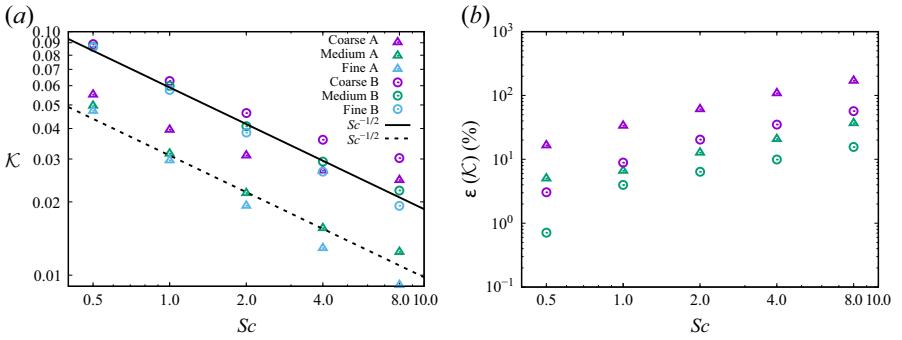

Figure 11. Grid sensitivity analysis results from simulations of a reduced channel (four times smaller than the one analysed in the main body of the paper) used as a reference test. Coarse grid, $\Delta x^+ = 6.54$; medium grid, $\Delta x^+ = 3.27$; fine grid, $\Delta x^+ = 1.635$. Label A refers to simulations with diffusivity ratio $D_r = 1$, while label B refers to simulations with diffusivity ratio $D_r = (50, 100, 200, 400, 800)$. (*a*) Scaling of gas-transfer velocity, $\mathcal{K}$, as a function of Schmidt number, Sc. (*b*) Relative error, ϵ, of $\mathcal{K}$ with respect to the fine-grid results.

demonstrates improved accuracy with increasing resolution, ranging from approximately 1 % error at lower Schmidt numbers to about 10 %–20 % error at $Sc = 4$.

References

Arora, M. & Roe, P.L. 1997 A well-behaved tvd limiter for high-resolution calculations of unsteady flow. *J. Comput. Phys.* **132** (1), 3–11.

Batchelor, G.K. 1959 Small-scale variation of convected quantities like temperature in turbulent fluid part 1. General discussion and the case of small conductivity. *J. Fluid Mech.* **5** (1), 113–133.

Bernardini, M., Pirozzoli, S. & Orlandi, P. 2014 Velocity statistics in turbulent channel flow up to. *J. Fluid Mech.* **742**, 171–191.

Bird, R.B. 2002 Transport phenomena. *Appl. Mech. Rev.* **55** (1), R1–R4.

Bothe, D. & Fleckenstein, S. 2013 A volume-of-fluid-based method for mass transfer processes at fluid particles. *Chem. Engng Sci.* **101**, 283–302.

Boussinesq, J. 1905 Calcul du pouvoir refroidissant des fluides. *J. Math. Pures Appl.* **1**, 285–332.

Broecker, H.-C., Petermann, J. & Siems, W. 1978 The influence of wind on co2-exchange in a wind-wave tunnel, including the effects of monolayers. *J. Mar. Res.* **4**, 36.

Calmet, I. & Magnaudet, J. 1998 High-Schmidt number mass transfer through turbulent gas–liquid interfaces. *Intl J. Heat Fluid Flow* **19** (5), 522–532.

Cano-Lozano, J.É C., Martinez-Bazan, C., Magnaudet, J. & Tchoufag, J. 2016 Paths and wakes of deformable nearly spheroidal rising bubbles close to the transition to path instability. *Phys. Rev. Fluids* **1** (5), 053604.

Chorin, A.J. 1968 Numerical solution of the Navier–Stokes equations. *Math. Comput.* **22**, 745–762.

Clift, R., Grace, J.R. & Weber, M.E. 2005 *Bubbles, Drops, and Particles*. Courier Corporation.

Colombet, D., Legendre, D., Cockx, A., Guiraud, P., Risso, F., Daniel, C. & Galinat, S. 2011 Experimental study of mass transfer in a dense bubble swarm. *Chem. Engng Sci.* **66** (14), 3432–3440.

Colombet, D., Legendre, D., Risso, F., Cockx, A. & Guiraud, P. 2015 Dynamics and mass transfer of rising bubbles in a homogenous swarm at large gas volume fraction. *J. Fluid Mech.* **763**, 254–285.

Crialesi-Esposito, M., Chibbaro, S. & Brandt, L. 2023 The interaction of droplet dynamics and turbulence cascade. *Commun. Phys.* **6** (1), 5.

Dani, A., Guiraud, P. & Cockx, A. 2007 Local measurement of oxygen transfer around a single bubble by planar laser-induced fluorescence. *Chem. Engng Sci.* **62** (24), 7245–7252.

Darmana, D., Deen, N.G. & Kuipers, J.A.M. 2006 Detailed 3d modeling of mass transfer processes in two-phase flows with dynamic interfaces. *Chem. Engng Technol.: Ind. Chem.-Plant Equipm.-Process Engng-Biotechnol.* **29** (9), 1027–1033.

Deane, G.B. & Stokes, M.D. 2002 Scale dependence of bubble creation mechanisms in breaking waves. *Nature* **418** (6900), 839–844.

Deike, L. 2022 Mass transfer at the ocean–atmosphere interface: the role of wave breaking, droplets, and bubbles. *Annu. Rev. Fluid Mech.* **54**, 191–224.

DEIKE, L., MELVILLE, W.K. & POPINET, S. 2016 Air entrainment and bubble statistics in breaking waves. *J. Fluid Mech.* **801**, 91–129.
DEISING, D., BOTHE, D. & MARSCHALL, H. 2018 Direct numerical simulation of mass transfer in bubbly flows. *Comput. Fluids* **172**, 524–537.
DEISING, D., MARSCHALL, H. & BOTHE, D. 2016 A unified single-field model framework for volume-of-fluid simulations of interfacial species transfer applied to bubbly flows. *Chem. Engng Sci.* **139**, 173–195.
DI GIORGIO, S., PIROZZOLI, S., IAFRATI, A. 2022 On coherent vortical structures in wave breaking. *J. Fluid Mech.* **947**, A44.
DI GIORGIO, S., PIROZZOLI, S., IAFRATI, A. 2024 Evaluation of advection schemes and surface tension model for algebraic and geometric vof multiphase flow solvers. *J. Comput. Phys.* **499**, 112717.
DI GIORGIO, S., PIROZZOLI, S. & IAFRATI, A. 2025 Air entrainment and gas transfer in wave breaking events. *Geophys. Res. Lett.* **52** (15), e2025GL114907.
DODD, M.S., MOHADDES, D., FERRANTE, A. & IHME, M. 2021 Analysis of droplet evaporation in isotropic turbulence through droplet-resolved dns. *Intl J. Heat Mass Transfer* **172**, 121157.
EMERSON, S. & BUSHINSKY, S. 2016 The role of bubbles during air-sea gas exchange. *J. Geophys. Res. Oceans* **121** (6), 4360–4376.
FARSOIYA, P.K., POPINET, S. & DEIKE, L. 2021 Bubble-mediated transfer of dilute gas in turbulence. *J. Fluid Mech.* **920**, A34.
FRANCOIS, J., DIETRICH, N., GUIRAUD, P. & COCKX, A. 2011 Direct measurement of mass transfer around a single bubble by micro-plifi. *Chem. Engng Sci.* **66** (14), 3328–3338.
HANRATTY, T.J. 1991 Effect of gas flow on physical absorption. In *Air-Water Gas Transfer* (ed. S.C. Wilhelms & J.S. Gulliver), pp. 10–13. ASCE.
HAROUN, Y., LEGENDRE, D. & RAYNAL, L. 2010 Volume of fluid method for interfacial reactive mass transfer: application to stable liquid film. *Chem. Engng Sci.* **65** (10), 2896–2909.
HASEGAWA, Y. & KASAGI, N. 2003 Turbulent mass transfer across an air-water interface at high Schmidt numbers. *Trans. JSME B* **69**, 824–832.
HASEGAWA, Y. & KASAGI, N. 2006 Dependency of local scalar flux on surface divergence at a turbulent air-water interface. *Nippon Kikai Gakkai Ronbunshu B Hen (Trans. Jpn. Soc. Mech. Engng Part B) (Japan)* **18** (5), 1206–1213.
HASEGAWA, Y. & KASAGI, N. 2008 Systematic analysis of high Schmidt number turbulent mass transfer across clean, contaminated and solid interfaces. *Intl J. Heat Fluid Flow* **29** (3), 765–773.
HERLINA, H. & WISSINK, J.G. 2019 Simulation of air–water interfacial mass transfer driven by high-intensity isotropic turbulence. *J. Fluid Mech.* **860**, 419–440.
HIDMAN, N., STRÖM, H., SASIC, S. & SARDINA, G. 2023 Assessing passive scalar dynamics in bubble-induced turbulence using direct numerical simulations. *J. Fluid Mech.* **962**, A32.
IWANO, K., TAKAGAKI, N., ILYASOV, E., KUROSE, R. & KOMORI, S. 2012 Effect of fetch and entrained bubbles on mass transfer velocity across the wind-driven air-water interface with wave breaking. In *Proceedings of The 8th KSME-JSME Thermal and Fluids Engineering Conference*, pp. 18–21.
IWANO, K., TAKAGAKI, N., KUROSE, R. & KOMORI, S. 2013 Mass transfer velocity across the breaking air–water interface at extremely high wind speeds. *Tellus B: Chem. Phys. Meteorol.* **65** (1), 21341.
JIA, H., XIAO, X. & KANG, Y. 2019 Investigation of a free rising bubble with mass transfer by an arbitrary Lagrangian–Eulerian method. *Intl J. Heat Mass Transfer* **137**, 545–557.
JÄHNE, B. & HAUSSECKER, H. 1998 Air-water gas exchange. *Annu. Rev. Fluid Mech.* **30**, 443–468.
JÄHNE, B., MÜNNICH, K.O., BÖSINGER, R., DUTZI, A., HUBER, W. & LIBNER, P. 1987 On the parameters influencing air-water gas exchange. *J. Geophys. Res.* **92** (C2), 1937–1949.
JÄHNE, B., WAIS, T., MEMERY, L., CAULLIEZ, G., MERLIVAT, L., MÜNNICH, K.O. & COANTIC, M. 1985 He and Rn gas exchange experiments in the large wind-wave facility of imst. *J. Geophys. Res.* **90** (C6), 11989–11997.
KOKAL, S. 2005 Crude-oil emulsions: a state-of-the-art review. *SPE Prod. Facil.* **20** (01), 5–13.
KOMORI, S., KUROSE, R., IWANO, K., UKAI, T. & SUZUKI, N. 2010 Direct numerical simulation of wind-driven turbulence and scalar transfer at sheared gas–liquid interfaces. *J. Turbulence* **11**, N32.
KUERTEN, J.G.M. 2016 Point-particle dns and les of particle-laden turbulent flow-a state-of-the-art review. *Flow Turbul. Combust.* **97**, 689–713.
KUMAR, A. & HARTLAND, S. 1999 Correlations for prediction of mass transfer coefficients in single drop systems and liquid–liquid extraction columns. *Chem. Engng Res. Des.* **77** (5), 372–384.
LEVICH, V.G. 1962 *Physicochemical Hydrodynamics*, Prentice-Hall International Series in the Physical and Chemical Engineering Sciences. Prentice-Hall.
LISS, P.S. 1973 Processes of gas exchange across an air-water interface. *Deep Sea Res. Oceanogr. Abstracts* **20**, 221–238.

LISS, P.S. & SLATER, P.G. 1974 Flux of gases across the air-sea interface. *Nature* **247** (5438), 181–184.
MANGANI, F., ROCCON, A., ZONTA, F. & SOLDATI, A. 2024 Heat transfer in drop-laden turbulence. *J. Fluid Mech.* **978**, A12.
MAXWORTHY, T., GNANN, C., KÜRTEN, M. & DURST, F. 1996 Experiments on the rise of air bubbles in clean viscous liquids. *J. Fluid Mech.* **321**, 421–441.
MERLIVAT, L. & MEMERY, L. 1983 Gas exchange across an air-water interface: experimental results and modeling of bubble contribution to transfer. *J. Geophys. Res.* **88** (C1), 707–724.
MOORE, D.W. 1965 The velocity of rise of distorted gas bubbles in a liquid of small viscosity. *J. Fluid Mech.* **23** (4), 749–766.
MÉÈS, L., GROSJEAN, N., MARIÉ, J.-L. & FOURNIER, C. 2020 Statistical Lagrangian evaporation rate of droplets released in a homogeneous quasi-isotropic turbulence. *Phys. Rev. Fluids* **5** (11), 113602.
ORLANDI, P. 2012 *Fluid Flow Phenomena: A Numerical Toolkit*, vol. 55. Springer Science & Business Media.
PELUSI, F., ASCIONE, S., SBRAGAGLIA, M. & BERNASCHI, M. 2023 Analysis of the heat transfer fluctuations in the Rayleigh–Bénard convection of concentrated emulsions with finite-size droplets. *Soft Matt.* **19** (37), 7192–7201.
PIROZZOLI, S., DI GIORGIO, S. & IAFRATI, A. 2019 On algebraic tvd-vof methods for tracking material interfaces. *Comput. Fluids* **189**, 73–81.
PIROZZOLI, S. & ORLANDI, P. 2021 Natural grid stretching for dns of wall-bounded flows. *J. Comput. Phys.* **439**, 110408.
POPE, S.B. 2001 Turbulent flows. *Meas. Sci. Technol.* **12** (11), 2020–2021.
PROCACCI, D., AROSEMENA, A.A., DI GIORGIO, S. & SOLSVIK, J. 2026 Turbulence anisotropy modulation in bubble-laden channel flow: a numerical study. *Intl J. Multiphase Flow* **195**, 105505.
PROCACCI, D., ROCCON, A., SOLSVIK, J. & SOLDATI, A. 2025 Heat transfer in drop-laden low-Prandtl-number channel turbulence. *J. Fluid Mech.* **1015**, A19.
RISSO, F. 2018 Agitation, mixing, and transfers induced by bubbles. *Annu. Rev. Fluid Mech.* **50** (1), 25–48.
ROCCON, A., ZONTA, F. & SOLDATI, A. 2023 Phase-field modeling of complex interface dynamics in drop-laden turbulence. *Phys. Rev. Fluids* **8**, 090501.
ROGHAIR, I. 2012 Direct numerical simulations of hydrodynamics and mass transfer in dense bubbly flows. PhD thesis 1 (research tu/e/graduation tu/e), Chemical Engineering and Chemistry.
ROSSI, D., DI GIORGIO, S. & PIROZZOLI, S. 2025 Comparative analysis of volume of fluid and phase–field methods for numerical simulations of two-phase flows. *Intl J. Multiphase Flow* **189**, 105245.
SANDER, R. 2023 Compilation of henry's law constants (version 5.0. 0) for water as solvent. *Atmos. Chem. Phys.* **23** (19), 10901–12440.
SCAPIN, N.Ò, BARBA, D., FEDERICO, L., GIANDOMENICO, R., EDOARDO, M., DUWIG, C. & BRANDT, L. 2022 Finite-size evaporating droplets in weakly compressible homogeneous shear turbulence. *J. Fluid Mech.* **934**, A15.
STANDART, G. 1964 The mass, momentum and energy equations for heterogeneous flow systems. *Chem. Engng Sci.* **19** (3), 227–236.
TAKAGAKI, N., KUROSE, R., KIMURA, A. & KOMORI, S. 2016 Effect of Schmidt number on mass transfer across a sheared gas–liquid interface in a wind-driven turbulence. *Sci. Rep.* **6** (1), 37059.
TAKAGAKI, N., KUROSE, R., TSUJIMOTO, Y., KOMORI, S. & TAKAHASHI, K. 2015 Effects of turbulent eddies and Langmuir circulations on scalar transfer in a sheared wind-driven liquid flow. *Phys. Fluids* **27** (1), 016603.
THAN, P., PREZIOSI, L., JOSEPHL, D.D. & ARNEY, M. 1988 Measurement of interfacial tension between immiscible liquids with the spinning road tensiometer. *J. Colloid Interface Sci.* **124** (2), 552–559.
TRYGGVASON, G., SCARDOVELLI, R. & ZALESKI, S. 2011 *Direct Numerical Simulations of Gas–liquid Multiphase Flows*. Cambridge University Press.
WANNINKHOF, R., ASHER, W.E., HO, D.T., SWEENEY, C. & MCGILLIS, W.R. 2009 Advances in quantifying air-sea gas exchange and environmental forcing. *Ann. Rev. Mar. Sci.* **1** (1), 213–244.
WEYMOUTH, G.D. & YUE, D.K.-P. 2010 Conservative volume-of-fluid method for free-surface simulations on cartesian-grids. *J. Comput. Phys.* **229** (8), 2853–2865.
WYLOCK, C., COLINET, P. & HAUT, B. 2012 Gas absorption into a spherical liquid droplet: numerical and theoretical study. *J. Chem. Engng* **207**, 851–864.
XU, J.H., TAN, J., LI, S.W. & LUO, G.S. 2008 Enhancement of mass transfer performance of liquid–liquid system by droplet flow in microchannels. *Chem. Engng J.* **141** (1–3), 242–249.